FACULDADE DE ENGENHARIA DA UNIVERSIDADE DO PORTO

Mechanical Characterization of Auxetic Mesh Implant Designs Tested with Sow Vaginal Tissue

Inês Martins Mota

MASTER'S DISSERTATION

U.PORTO

FEUP FACULDADE DE ENGENHARIA UNIVERSIDADE DO PORTO

Biomedical Engineering Master's Degree

Supervisor: Dra. Maria Elisabete Teixeira da Silva

Co-Supervisor: Nuno Miguel Araújo Ferreira

June 2026

Abstract

Pelvic organ prolapse (POP) is a common clinical condition that significantly affects the quality of life of millions of women worldwide. Synthetic polypropylene meshes, previously used in the surgical treatment of this condition, have gradually been phased out due to the complications associated with their use, notably excessive stiffness, tissue erosion, chronic pain and an inflammatory response. As an alternative, biodegradable meshes have been developed that are capable of providing temporary mechanical support and promoting tissue regeneration, thereby reducing the risk of long-term complications.

In this context, the aim of this study was to evaluate the mechanical properties of biodegradable polycaprolactone (PCL) meshes with auxetic geometries produced by Melt Electrowriting (MEW). Auxetic structures, characterized by a negative Poisson's ratio, have the ability to expand laterally when subjected to tensile stresses, offering advantages such as greater conformability, improved stress redistribution and more efficient adaptation to the physiological movements of tissues.

Two distinct geometries were developed, re-entrant honeycomb and double arrowhead, and subsequently evaluate through uniaxial and ball burst tests. In the uniaxial tests, the meshes and the vaginal tissue were assessed separately, whereas in the ball burst tests, the meshes alone, the vaginal tissue alone and the tissue-mesh system were tested.

The uniaxial tensile tests revealed a marked directional dependence of the mechanical response for both geometries, with greater stiffness and tensile strength observed in the "auxetic direction" and greater deformability in the "non-auxetic direction"**.** Among the structures studied, the double arrowhead geometry exhibited the highest values of stiffness and tensile strength, whilst the re-entrant honeycomb geometry demonstrated greater deformability.

In ball burst tests, both geometries demonstrated the ability to mechanically reinforce vaginal tissue, significantly increasing the maximum load borne compared with unreinforced tissue. The re-entrant honeycomb geometry enabled the tissue's load-bearing capacity to be approximately doubled, whilst the double arrowhead geometry performed better, combining

increased mechanical strength with a substantially higher capacity for deformation. A comparison with conventional geometries reported in the literature showed that, although the latter exhibit higher maximum loads, the double arrowhead geometry demonstrates a greater capacity to accommodate deformation, a characteristic that is potentially advantageous for applications in the treatment of pelvic organ prolapse.

Overall, the results demonstrate the potential of PCL auxetic meshes for vaginal reinforcement applications, with the double arrowhead geometry emerging as the most promising design due to its favourable balance between mechanical support, deformability and biomechanical compatibility with vaginal tissue.

Keywords: Pelvic organ prolapse (POP); Auxetic structures; Polycaprolactone (PCL); Melt Electrowriting (MEW); Biodegradable meshes; Vaginal tissue; Mechanical characterization.

Resumo

O prolapso dos órgãos pélvicos é uma condição clínica frequente que afeta significativamente a qualidade de vida de milhões de mulheres em todo o mundo. As malhas sintéticas de polipropileno, anteriormente utilizadas no tratamento cirúrgico desta patologia, foram progressivamente abandonadas devido às complicações associadas à sua utilização, nomeadamente rigidez excessiva, erosão tecidular, dor crónica e resposta inflamatória. Como alternativa, têm vindo a ser desenvolvidas malhas biodegradáveis capazes de fornecer suporte mecânico temporário e promover a regeneração dos tecidos, reduzindo o risco de complicações a longo prazo.

Neste contexto, o presente trabalho teve como objetivo caracterizar mecanicamente malhas biodegradáveis de policaprolactona (PCL), um polímero biocompatível e bioabsorvível, com geometrias auxéticas produzidas por *Melt Electrowriting* (MEW). As estruturas auxéticas, caracterizadas por apresentarem coeficiente de Poisson negativo, possuem a capacidade de expandir lateralmente quando sujeitas a esforços de tração, oferecendo vantagens como maior conformabilidade, melhor redistribuição de tensões e uma adaptação mais eficiente aos movimentos fisiológicos dos tecidos.

Foram desenvolvidas duas geometrias distintas, *re-entrant honeycomb* e *double arrowhead*, posteriormente caracterizadas através de ensaios uniaxiais e de *ball burst*. Nos ensaios uniaxiais, as malhas e o tecido vaginal foram avaliados isoladamente, enquanto nos ensaios de *ball burst* foram testadas as malhas isoladas, o tecido vaginal isolado e os sistemas tecido-malha.

Os resultados dos ensaios uniaxiais evidenciaram um comportamento anisotrópico para ambas as geometrias, observando-se maior rigidez e resistência na “direção auxética” e maior deformabilidade na “direção não auxética”. Entre as estruturas estudadas, a geometria *double arrowhead* apresentou os maiores valores de rigidez e resistência à tração, enquanto a geometria *re-entrant honeycomb* revelou maior capacidade de deformação.

Nos ensaios de *ball burst*, ambas as geometrias demonstraram capacidade para reforçar mecanicamente o tecido vaginal, aumentando significativamente a carga máxima suportada relativamente ao tecido não reforçado. A geometria *re-entrant honeycomb* permitiu aproximadamente duplicar a capacidade resistente do tecido, enquanto a geometria *double arrowhead* apresentou um desempenho superior, combinando um aumento da resistência mecânica com uma capacidade de deformação substancialmente mais elevada. A comparação com geometrias convencionais reportadas na literatura demonstrou que, embora estas apresentem cargas máximas superiores, a geometria *double arrowhead* exibe uma maior capacidade para acomodar deformações, característica potencialmente vantajosa para aplicações no tratamento do prolapso dos órgãos pélvicos.

De um modo geral, os resultados obtidos demonstram que as malhas auxéticas de PCL possuem potencial para aplicações de reforço vaginal, destacando-se a geometria *double arrowhead* como a solução mais promissora devido ao equilíbrio favorável entre suporte mecânico, deformabilidade e compatibilidade biomecânica com o tecido vaginal.

Palavras-chave: Prolapso de órgãos pélvicos; Estruturas auxéticas; Policaprolactona (PCL); Melt Electrowriting (MEW); Malhas biodegradáveis; Tecido vaginal; Caracterização mecânica.

Acknowledgements

First and foremost, I would like to express my deepest gratitude to my family, whose unconditional love, encouragement, and support have been a constant source of strength throughout this journey. I am also profoundly thankful to my boyfriend, for his patience, understanding, and motivation during the most challenging moments of this work.

I am sincerely grateful to my supervisor, Prof. Maria Elisabete Teixeira da Silva, for her invaluable guidance, expertise, and continuous encouragement, which were fundamental to the successful development of this dissertation. I also wish to thank my co-supervisor, Engineer Nuno Miguel Araújo Ferreira, for his constructive insights, availability, and valuable contributions that greatly enriched this work.

A special word of appreciation goes to Joana and Francisca, members of the research group that welcomed me during this dissertation. Their support and assistance in the laboratory work were essential, and I am truly grateful for their generosity and collaboration.

Contents

List of Figures

Abbreviations

3D   Three-dimensional

AM   Additive Manufacturing

CNC   Computer Numerical Control

CT   Computed Tomography

DLP   Digital light processing

EBM   Electron Beam Melting

ECM   Extracellular matrix

ES   Electrospinning

FDA   Food and Drug Administration

FDM   Fused Deposition Modeling

FFF   Fused Filament Fabrication

G-code   Geometric Code

GH   Genital hiatus

LOM   Laminated Object Manufacturing

MES   Melt Electrospinning

MEW   Melt Electrospinning Writing

MRI   Magnetic resonance imaging

PB   Perineal body

PCL   Polycaprolactone

PEG Polyethylene Glycol

PET Polyethylene Terephthalate

PFD Pelvic Floor Dysfunction

PFM Pelvic Floor Muscles

PGA Polyglycolic Acid

PLA Polylactic Acid

PLGA Poly (Lactic-co-Glycolic Acid)

POP Pelvic Organ Prolapse

POP-Q Pelvic Organ Prolapse Quantification

PP Polypropylene

PTFE Polytetrafluoroethylene

PU Polyurethane

PVDF Polyvinylidenefluoride

SES Solution Electrospinning

SLA Stereolithography

SLM Selective Laser Melting

SLS Selective Laser Sintering

TVL Total vaginal length

Chapter 1

Introduction

The dissertation's introductory elements are covered in this chapter. First, the history and causes of pelvic organ prolapse (POP) are discussed, along with the issues surrounding the synthetic meshes used to treat it. Then, by employing biodegradable materials to produce meshes, 3D printing is proposed to get around these issues. The dissertation's primary and objectives are next outlined. This chapter also contains the dissertation's framework.

1.1 Motivation

POP is one of the most prevalent types of pelvic floor dysfunction (PFD), in which one or more pelvic organs slip out of their usual place and bulge into the vagina. This is a common condition in which pelvic tissues descend into the vagina as a result of ligament or muscle failure/weakening. This dysfunction occurs due to several factors, such as pregnancy and age, affecting the quality of life of women.

This issue affects 2.9% to 8% of the female population, and women have a 12.6% lifetime probability of requiring surgery to treat prolapse [1].

This illness affects 41% of women over 60 [2], with a lifetime frequency of 30% to 50%. By the age of 79, 11% to 12% of women with an average life expectancy may require surgical intervention for prolapse or incontinence, with a 29% re-operation rate [3]. It is predicted that 10 to 15% of women in developed nations may undergo POP repair surgery during their lifetime [4].

By 2050, the number of women with POP is predicted to rise by 46%. The treatment options for this problem vary depending on the severity of the prolapse, but in most severe cases, surgery is advised [5]. Each year, approximately 7,000 women in Portugal are affected by POP.

This figure is predicted to rise by 40% over the next 40 years due to the increased average age of the female population [6].

In the early days, specifically in the 1970s, gynecologists used free grafts for pelvic floor reconstruction surgery, which required cutting them into different shapes, which was not a safe practice. Then, medical device manufacturers began to develop mesh-based kits in various shapes and sizes. The first prosthesis for POP treatment was authorized by the Food and Drug Administration (FDA) in 2002. Since then, research into these meshes has advanced to the point that synthetic surgical meshes have been developed as an alternative to biological grafts [7].

As such, the Therapeutic Goods Administration reported that between 2005 and 2013, 3.7 million synthetic meshes were implanted worldwide. However, the insertion of these meshes has been associated with graft-related problems, including vaginal erosion, infection, pain, and discomfort [8]. The complications described above are due to their tendency to adhere to the viscera and induce a heightened inflammatory response, as well as their increased rigidity over time, causing weakening of the surrounding tissues [7].

That being said, in 2019, the FDA banned the manufacture and distribution of transvaginal synthetic meshes for POP treatment in the United States and given the prevalence of POP, lowering reoperation rates and complications is critical for improving patient outcomes [9].

Previous studies on the unique characteristics that surgical meshes must have for the treatment of POP have revealed a complex relationship between the geometry and mechanical behavior of a mesh-like structure.

To overcome this problem, biodegradable meshes have been attracting the attention of researchers, as well as 3D printing to produce surgical meshes for POP treatment. Melt electrospinning writing (MEW), a type of electrospinning (ES) technique used in 3D printing, has proven to be an effective method for creating intricate and durable structures. This process can produce nanofibers from biodegradable polymers such as polycaprolactone (PCL), which is FDA-approved for clinical usage in biomedical applications.

The combination of electrospinning technology with 3D printing has demonstrated significant advantages in the treatment of implant-related complications, as it allows the creation of complex and optimized structures through the controlled and precise deposition of fibers on a small scale. As such, fusion electrospinning offers the ability to tailor material properties for customized constructions, using biodegradable polymers and their blends to increase biocompatibility and production efficiency [10].

1.2 Objectives

The main objective of this dissertation was to design, fabricate, and mechanically evaluate biodegradable auxetic meshes produced by MEW for potential application in POP repair. Specifically, two auxetic geometries, the *Re-entrant honeycomb* and the *Double Arrowhead* structures were investigated due to their unique deformation mechanisms and ability to provide improved mechanical performance.

The study aimed to (i) evaluate the reproducibility of the MEW printing process in producing meshes with controlled thickness and pore size, (ii) assess the uniaxial tensile and multiaxial (ball burst) mechanical properties of the meshes, (iii) compare the performance of the meshes with commercial polypropylene-based implants (*Restorelle*) and with sow vaginal tissue, and (iv) analyze the interaction between mesh and tissue to determine their combined mechanical response. Through these objectives, this work sought to determine whether MEW-fabricated auxetic meshes could represent a safer and more effective alternative to conventional synthetic implants used in POP treatment.

1.3 Dissertation Structure

This dissertation is structured as follows:

- **Chapter 2**: Describes the anatomy of the female pelvis and pelvic floor dysfunction, namely POP. It also discusses the present therapies for this illness and future therapy options.
- **Chapter 3**: Provides an overview of additive manufacturing, including subtypes of electrospinning processes, MEW applications, and benefits. This chapter also characterizes auxetic structures, referring to the variety of materials used, the different manufacturing techniques, and their applicability in biomedical devices, also bridging the gap with the treatment of POP.
- **Chapter 4**: This chapter provides an overview of the approach, including the MEW prototype, materials, and procedures (mechanical characterization) utilized to meet the dissertation's objectives.
- **Chapter 5**: Presentation of the results obtained in the mechanical characterization of PCL auxetic meshes printed using MEW (uniaxial tests and

ball burst tests). These results are analyzed and discussed based on studies in literature on this topic.

- **Chapter 6**: This chapter presents the main findings and suggestions for future work.

Chapter 2

Female Pelvis: anatomy and disfunction

The following chapter addresses the theoretical foundations that enable understanding of the disease underlying the work carried out. First, the anatomy of the female pelvic area is described, together with the characterization of pelvic organ prolapse, i.e., its context, symptoms, classification, diagnosis, and, finally, existing treatments.

Finally, this chapter also presents an analysis of existing synthetic surgical meshes and the development of biodegradable meshes.

2.1 Anatomy of the Female Pelvis

The pelvis is located in the center of the body and separates the lumbar portion of the abdomen from the inferior members [11]. It includes the bony pelvis or pelvic girdle, the pelvic cavity, the pelvic floor, and the perineum [6]. The pelvis serves a variety of important functions, including giving structural support and stability to all movements, such as walking or standing, as well as supporting all abdominal organs and, in the case of a woman, supporting childbirth [11].

The male pelvis is heavier and thicker than the female pelvic. The male pelvis has a heart-shaped inlet, but the female pelvis is often more circular and bigger, which might result in pelvic floor weakness [12]**.** Figure 1 depicts the shape of the male and female pelvis. Women have a greater pubic arch (80º - 85º) than males (50º - 60º) [12].

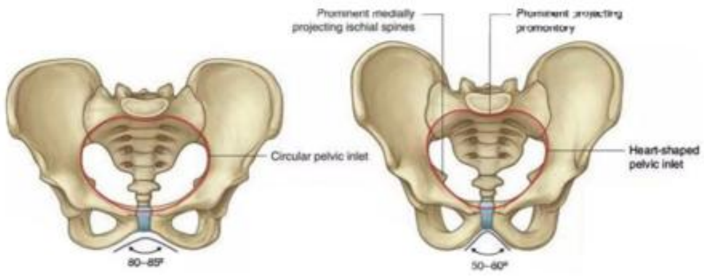

***Figure 1** Structure of bone pelvis in women (left) and men (right)* [12].

The sacrum, ilium, pubis, and ischium make up the bony pelvis. The pelvic brim separates it into two parts, acting as an imaginary line that divides them. The false or greater pelvis is located above this line and includes the lower lumbar vertebra, abdominal cavity, and portion of the small intestine. The true or lesser pelvis, located below the line, houses the reproductive organs and the distal section of the urinary system [13].

Following on from what was mentioned above, the bony pelvis, often called the pelvic girdle, links the spinal column and two femora. The pelvis consists of the right and left hip bones, as well as the sacrococcygeal section of the spinal column. It includes the sacrum, coccyx, and two hip bones. Each hip bone is made from the ischium, pubis, and ilium [14]. The bony pelvis has four articulations: the symphysis pubis, which connects the hip bones anteriorly; two sacroiliac joints, where the hip bone's medial aspect articulates with the sacrum's lateral aspect on both sides and the sacrococcygeal joint, which connects the inferior end of the sacrum to the upper surface of the coccyx [6]. Figure 2 shows the anterior view of the pelvic bones.

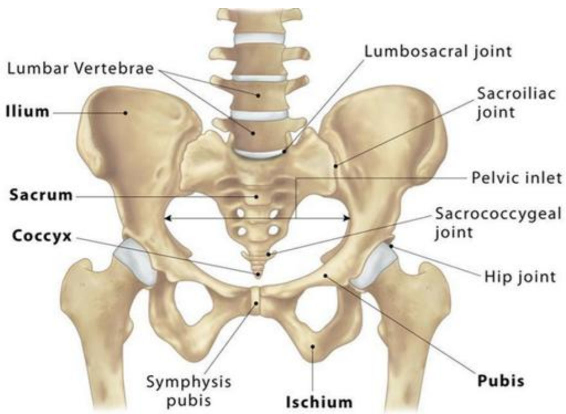

***Figure 2** Anterior view of the pelvic bones* [8].

Between the abdominal cavity and the pelvic floor lies the pelvic cavity, which is a hollow bony structure that makes up the area inside the pelvic bones. This cavity includes several organs of the gastrointestinal tract, musculoskeletal system, and urogenital system, such as the rectum, uterus, ovaries, fallopian tubes, vagina, urethra, bladder and ureters, as well as vessels, nerves, and lymphatic vessels [6]. Figure 3 illustrates the organs of the female pelvic cavity.

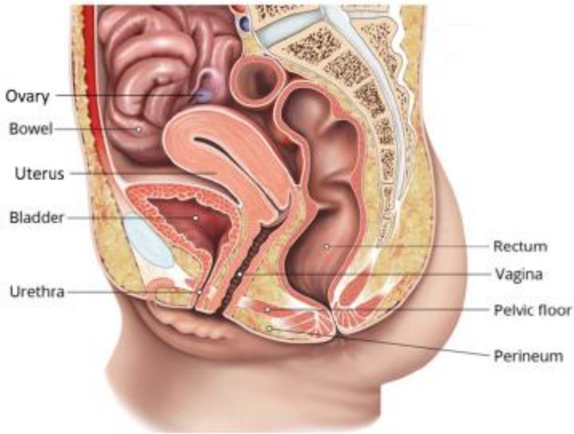

Figure 3 *Female pelvic cavity organs* [15].

The pelvic floor consists of the muscles, ligaments and fascia that support the organs in the pelvic cavity. The pelvic floor muscles (PFM) not only support the organs but also offer the flexibility required for physiological activities. The principal muscles are the levator ani and the coccygeus, which are found bilaterally. The levator ani consists of the pubococcygeus, puborectal, and iliococcygeus muscles and accounts for the majority of the PFM. The coccygeus is a minor muscle in the rear of the pelvis [16][17].

The pelvic muscles have two layers: superficial and deep. The deep pelvic floor is made up of iliococcygeal, puborectal and pubovisceral muscles. The superficial muscles include the ischiocavernosus, bulbospongiosus and superficial transverse perineal muscles [18].

The perineum is a diamond-shaped region that connects the pubic symphysis to the coccyx. It is composed of the posterior anal triangle and the anterior urogenital triangle, which correlate to the external genitalia, the vulva [18]. Figure 4 describes the female pelvic floor in detail.

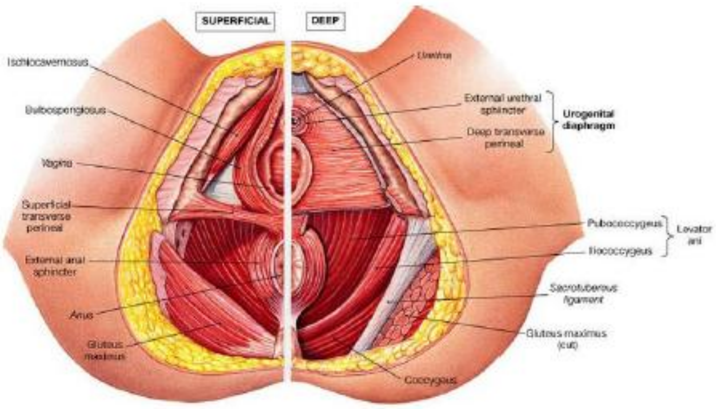

Figure 4 *Female pelvic floor* [6].

2.2 Pelvic Floor Dysfunctions: Pelvic Organ Prolapse

Pelvic floor dysfunctions encompass a range of conditions, including urinary and anal incontinence, sexual dysfunctions and POP, which constitutes the primary focus of this dissertation. These disorders exert a considerable impact not only on women's physical health but also on their psychological well-being [19].

POP is characterized by the descent of one or more pelvic organs (uterus, vagina, bladder or bowel) into the vaginal canal, resulting from the weakening of the pelvic floor's supportive structures [15][20]. Such support is primarily provided by fascia and ligaments, whose mechanical integrity depends largely on the extracellular matrix (ECM) of the connective tissue. The ECM is composed mainly of collagen, elastin, proteoglycans and glycoproteins, with collagen playing a pivotal role in structural support [21].

Evidence indicates that collagen types I and III are the predominant forms within the female pelvic floor. Type I collagen contributes to tissue stiffness, whereas type III collagen is associated with elasticity. Consequently, reductions in these collagen types compromise the mechanical strength of the pelvic floor. Furthermore, women affected by POP often present with reduced vaginal wall thickness, a phenomenon attributed to diminished levels of collagen, elastin and smooth muscle cells [21].

Some of these supporting tissues include the levator ani and coccygeus muscles, and it has been found that women with POP have a decrease in the thickness of the levator ani muscle. The perineal body is another important component that might cause POP if its strength is diminished. The types of pelvic organ prolapse, shown in Figure 5, differ according to the pelvic structures involved: Upper vaginal prolapse (**Uterus and Vaginal vault**: after hysterectomy, when the top of the vagina falls); Anterior vaginal wall prolapse (**Cystocele**: bladder descends; **Urethrocele**: urethra descends; **Paravaginal defect**: pelvic fascia defect); and Posterior vaginal wall prolapse (**Enterocele**: small bowel descends; **Rectocele**: rectum descends; **Perineal deficiency**).

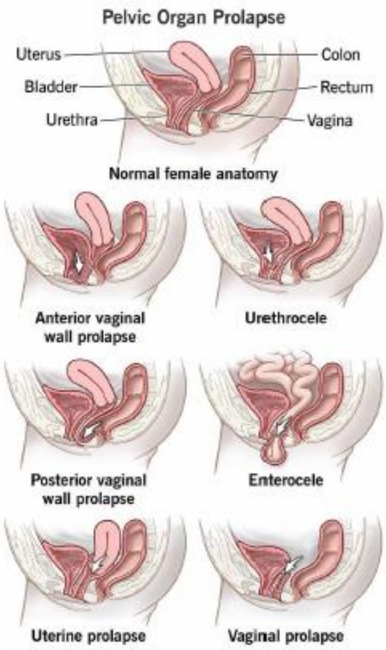

Figure 5 *Types of pelvic organ prolapse* [6].

POP is closely linked to physiological events such as pregnancy, vaginal delivery, menopause and the natural aging process [20][22]. In addition to these factors, a hereditary component has been identified, with women who have a family history of POP presenting a higher likelihood of developing the condition themselves [21]. Given the progressive aging of the global population, the prevalence of POP is expected to rise significantly in the coming years [15][19]. Moreover, external factors that increase intra-abdominal pressure, such as chronic respiratory disorders, persistent constipation, obesity, or repetitive physical strain, are also recognized as major contributors to its onset [23].

Although the clinical manifestation of POP is heterogeneous, many patients report pelvic or vaginal discomfort, often accompanied by urinary, bowel or sexual dysfunctions [15][20][22][23]. Additional symptoms may include a sensation of pelvic heaviness, the perception of a bulge or protrusion emerging from the vaginal canal and lower back pain [20]. Beyond the physical repercussions, the condition frequently impairs sexual health and has a profound psychological impact, thereby diminishing overall quality of life [15]. These consequences highlight the importance of effective management strategies and the development of innovative therapeutic approaches aimed at improving patient outcomes.

2.2.1 Diagnosis and Classification

The diagnosis of pelvic organ prolapse is based predominantly on a physical pelvic examination, which may be supplemented by functional bladder tests and imaging tests [5]. To assess the severity of the condition, a quantification system called Pelvic Organ Prolapse Quantification (POP-Q) is used. This standardized method uses the hymen plane as a reference, with measurements recorded in centimeters. Values located above (or proximal to) the reference plane are expressed as negative numbers, while values below (or distal to) are recorded as positive.

POP-Q includes six anatomical measurement points (Aa, Ba, C, D, Ap, Bp), as well as additional parameters, including the genital hiatus (GH), total vaginal length (TVL), and perineal body (PB) (Figure 6). These values can be organized in a grid format to facilitate analysis. Based on this system, prolapse is classified into five distinct stages [6]:

Stage 0: no prolapse.

Stage 1: descent greater than 1 cm above the level of the hymen.

Stage 2: prolapse located up to 1 cm above or below the hymen.

Stage 3: exteriorization of the most distal point between 1 cm and less than 2 cm of the total vaginal length below the hymen.

Stage 4: almost complete vaginal eversion.

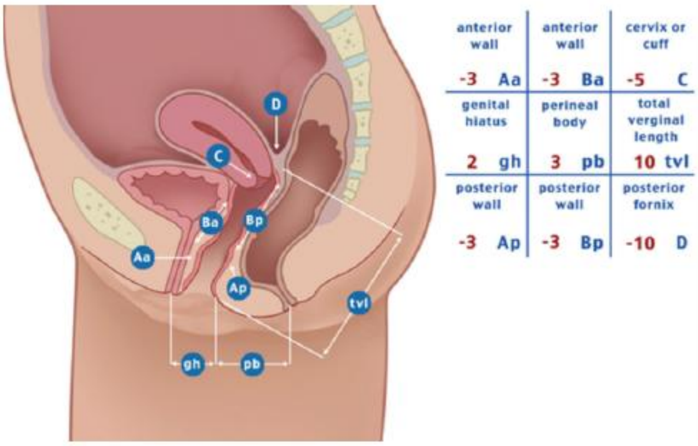

Figure 6 *Example of measurements using the POP-Q system* [6].

For a more in-depth characterization of the associated symptoms, complementary tests may be performed during the clinical evaluation, such as cystoscopy, defecography, magnetic resonance imaging (MRI), computed tomography (CT) or ultrasound, which help determine the severity of the prolapse [6].

2.3 Treatments for Pelvic Organ Prolapse

POP can be treated nonsurgically (conservative care and mechanical devices) or surgically (invasive) [1]. Treatment options are determined by factors such as prolapse severity, surgeon experience, symptoms and patient well-being [20].

2.3.1 Nonsurgical treatments

Conservative management is generally recommended for women with less advanced stages of prolapse, for those who wish to preserve fertility or for patients who decline surgical intervention [20]. Such approaches include behavioral modifications, such as weight reduction and the avoidance of heavy lifting as well as targeted pelvic floor muscle training. These strategies aim to alleviate symptoms, strengthen pelvic floor musculature and help prevent progression of the disorder, thereby potentially delaying the need for surgery [1].

Non-surgical alternatives also comprise the use of pessaries, removable devices designed to provide structural support in cases of prolapse [15]. Typically manufactured from medical-grade silicone [1], pessaries are often considered the first-line option when surgery is contraindicated or not acceptable to the patient [15]. However, their use may be limited in specific situations, such as when the vaginal length is insufficient or when the patient is unable to independently manage insertion and removal, as these devices must be periodically replaced [1].

2.3.2 Surgical treatments

It is estimated that between 6% and 18% of women diagnosed with POP eventually undergo surgical treatment [21]. In contrast to conservative management, surgical interventions aim to correct the underlying anatomical defects and various approaches may be employed [1]. The choice of procedure depends on multiple factors, including the severity of the prolapse, the specific symptoms presented by the patient, as well as the surgeon's expertise and clinical judgment [15]. Common surgical strategies include:

- **Restorative procedures** – reconstruction using the patient's native supportive tissues.
- **Compensatory procedures** – reinforcement with synthetic meshes or biological grafts.
- **Obliterative procedures** – partial or complete closure of the vaginal canal.

In most cases, conservative management proves insufficient, making invasive treatment necessary. Surgical repair is generally associated with low recurrence and complication rates, which is particularly relevant given the aging demographic [23]. Over a woman's lifetime, the probability of requiring prolapse surgery has been estimated between 12.6% and 20% [24], with the highest incidence observed in women aged 60 to 69 years [25]. Nevertheless, postoperative persistence of symptoms is reported in approximately 3% to 6% of cases [24].

2.3.2.1 Synthetic Meshes

Since the mid-1990s, compensatory surgical techniques involving the implantation of synthetic polymer meshes have been increasingly utilized in the management of POP [15]. Evidence suggests that the use of these meshes results in lower recurrence rates when compared with conventional fascial repair procedures [26]. These permanent implants are designed to provide additional support to the prolapsed organs, facilitating tissue recovery and pelvic muscle reinforcement, while minimizing damage to adjacent structures [27].

Synthetic surgical meshes are classed based on factors such as porosity, density, mechanical qualities, structure, filament type and absorption capacity, which can impact cell attachment and regeneration [28].

Meshes can be manufactured from absorbable, non-absorbable, or composite materials that combine both types. Common non-absorbable polymers include polypropylene (PP), polyethylene terephthalate (PET), polyvinylidene fluoride (PVDF) and polytetrafluoroethylene (PTFE) [6]. While these materials preserve their mechanical integrity over time, their rigidity can contribute to weakening of adjacent tissues and may increase the risk of postoperative infection. In contrast, absorbable meshes gradually degrade during the healing phase, typically avoiding infection but losing tensile strength as they are resorbed. Representative absorbable polymers include PCL, polylactic acid (PLA), poly(lactic-co-glycolic acid) (PLGA), and polyurethane (PU) [29].

From the perspective of filament composition, meshes may be classified as monofilament, consisting of a single continuous fiber, or multifilament, composed of several fibers bundled together. Multifilament configurations are generally more pliable and comfortable, yet their larger surface area and interstitial spaces facilitate bacterial colonization, thereby elevating the risk of infection. Monofilament meshes, on the other hand, exhibit greater stiffness but limited flexibility [30].

Structurally, meshes can be either woven or knitted. Knitted meshes are produced by looping a single filament into an interconnected network, whereas woven meshes are created by interlacing two sets of filaments perpendicularly [31]. Figure 7 illustrates woven and knitted fabric patterns.

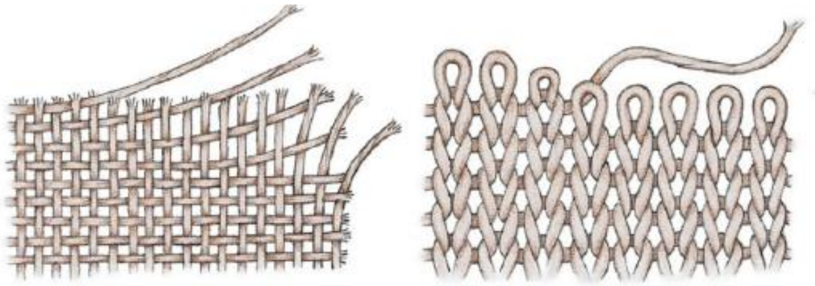

Figure 7 *Representation of woven (left) and knitted (right) meshes* [31].

The majority of commercially available meshes are knitted structures composed of various polymers, with PP being the most widely used [32]. PP is considered inert, biocompatible and capable of inducing only mild inflammatory reactions, while simultaneously promoting tissue integration and demonstrating high durability. However, one notable drawback is its tendency to adhere to visceral organs [27]. Among the latest clinical devices for POP repair is the *Restorelle®* mesh, developed by Coloplast [8]. This lightweight polypropylene mesh, with a density of 19 g/m^2, is suitable for both anterior and posterior vaginal prolapse repair [25][32].

Despite the advantages of synthetic mesh implants over traditional procedures that rely on native tissue, concerns regarding their safety persisted for many years. In 2008, the U.S. Food and Drug Administration (FDA) highlighted the elevated incidence of severe complications associated with transvaginal mesh use. Reported adverse outcomes included mesh exposure through the vaginal wall, infection, dyspareunia, inflammation and erosion of adjacent tissues. By 2011, the FDA concluded that such complications were not incidental, identifying mesh material, geometry and dimensions as potential contributing factors. Consequently, several products were withdrawn from the market, leading to a decline in the use of synthetic meshes for pelvic reconstructive surgery [13][15][23][24]. In 2019, the FDA imposed a nationwide ban on the sale and distribution of synthetic meshes for transvaginal POP repair in the United States [8].

The complications linked to these devices were influenced not only by the chemical composition of the polymers but also by their design and biomechanical performance. Polypropylene (PP) meshes, for instance, are known to stiffen over time, a phenomenon attributed to alterations in mechanical behavior following tissue integration and host response. Pore size also plays a critical role in mesh-tissue interaction. While larger pores encourage collagen deposition around the filaments, this process can lead to increased mesh stiffness and subsequent pain for the patient [33].

Among the withdrawn products was the *Restorelle®* mesh, which, along with many other synthetic devices, was removed from the U.S. market due to the FDA's stated lack of "reasonable assurance of safety and effectiveness" [32]. Some authors compared the mechanical behaviour of Restorelle® mesh and vaginal tissue using uniaxial tensile testing. The researchers found that the synthetic mesh is stiffer than the vaginal tissue, which will cause damage to the surrounding tissues, as well as inflammation and infections.

2.3.2.2 Biodegradable Meshes: The new solution

Given the significant complications associated with synthetic meshes, recent research has shifted toward the development of biodegradable alternatives. The main goals of these novel devices are to improve biocompatibility and minimize inflammatory reactions. Nevertheless, the precise set of properties that an ideal mesh should exhibit has not yet been clearly defined, which makes their design particularly challenging. From a biochemical standpoint, these materials should be inert, non-carcinogenic and resistant to both sterilization processes and microbial colonization. From a mechanical perspective, they must be capable of withstanding physiological loads and replicating the biomechanical behavior of native tissue under stress [27].

The primary target for these biodegradable implants is the surgical treatment of POP. For this reason, reproducing the beneficial characteristics of currently available synthetic meshes is advantageous. If it can be shown that biodegradable meshes provide comparable performance while overcoming the limitations of synthetic devices, they may represent a superior therapeutic option for pelvic organ prolapse repair.

Mesh porosity plays a crucial role in determining biocompatibility and the extent of host tissue integration [34]. Although the ideal pore size has not been clearly established, larger pores (> 1 mm) have been shown to reduce inflammatory responses, calcification and fistula formation, while also minimizing the risk of pore collapse [35]. Conversely, pores smaller than 1 mm are more prone to elicit inflammation and excessive connective tissue growth, which not only impairs tissue ingrowth but also leads to mesh encapsulation, factors collectively associated with postoperative pain [34].

For example, the now discontinued *Restorelle®* mesh was manufactured in different filament diameters (0.08, 0.16 and 0.24 mm) and pore sizes ranging between 1.6 and 2 mm [32]. Larger pores of this scale are known to facilitate host tissue integration, establishing 1–2 mm as a reference range for optimal porosity [32].

Mesh stiffness represents another critical design parameter. It is defined as the slope of the stress–strain relationship, indicating the resistance of the material to deformation under load. A stiffness that is too low compromises the ability of the implant to support overlying structures, whereas excessive stiffness increases the risk of erosion and tissue damage. This phenomenon is linked to the concept of stress shielding, whereby load-bearing tissues experience a reduction in mechanical strain once the mesh assumes part of the load, eventually leading to degeneration [27]. In addition, mesh geometry strongly influences mechanical performance under tension.

As most commercially available meshes are currently synthetic and knitted, recent studies have explored the potential of 3D printing technologies and biodegradable polymers for pelvic floor repair [2]. Although an ideal mesh design has yet to be established, advances in materials science and manufacturing techniques continue to offer promising strategies for overcoming the limitations of existing implants. Biodegradable polymers such as PCL, PLA, PLGA and PU have gained particular interest, as they may address the insufficient biocompatibility and suboptimal biomechanical behavior often associated with synthetic meshes [7].

Chapter 3

Additive Manufacturing Background

Additive manufacturing will be presented in this chapter, introducing the theoretical foundations related to the polymer processing technique used in the work developed. First, electrospinning (ES) and additive manufacturing (AM) technologies are discussed. Next, melt electrowriting (MEW) is addressed as a valuable tool for producing biodegradable meshes for the repair of POP. Studies related to the biomedical applications of MEW are also mentioned, as well as the motivation for using this type of additive in MEW-printed meshes. To conclude this chapter, it´s also addressed the topic of auxetic structures, characterizing them in terms of examples of auxetic designs, manufacturing methods, and referring to their potential in the field of biomedical engineering.

3.1 Additive Manufacturing

In recent years, AM, commonly referred to as 3D printing, has emerged as an innovative method of fabricating complex products. This technology relies on the principle of depositing successive layers of material under computer control to generate three-dimensional structures [36]. One of its main advantages is the high level of precision it offers, enabling manufacturers to tailor product design down to intricate details [37].

A broad spectrum of materials can be processed through AM, including polymers, metals, ceramics and composites [38]. Moreover, the available techniques are often classified according to the form of raw material employed [36], as summarized below:

- **Powder-based techniques**: Selective Laser Melting (SLM), Selective Laser Sintering (SLS), Electron Beam Melting (EBM).
- **Liquid-based techniques**: Stereolithography Apparatus (SLA), PolyJet.

- **Solid-based techniques**: Laminated Object Manufacturing (LOM), Fused Deposition Modeling (FDM)

3.1.1 Strengths and Limitations of Additive Manufacturing

In addition to material versatility, AM offers several advantages over conventional production methods. It is a relatively low-cost technique [38] that is particularly suited to small-scale, customized manufacturing, in contrast to traditional approaches that prioritize mass production [36]. Conventional methods generally involve multiple stages, operation, assembly and inspection, that require specialized expertise. AM circumvents this issue by enabling the simultaneous printing of integrated components, thereby eliminating the need for assembly and reducing overall costs. Further benefits include shorter production times, lower material waste and the capacity to fabricate geometrically complex structures that would be difficult to achieve with conventional processes [36].

However, AM is not without limitations. The surface finish of AM-produced parts is generally inferior to that obtained through traditional manufacturing. Rapid cooling during printing can also lead to distortions, which may adversely affect mechanical performance under load [39]. Additionally, the technique is constrained by printer size, which restricts the production of large monolithic structures and it is not optimized for mass production [39][40].

Although a wide range of materials, including polymers, metals, ceramics and composites, can be processed in powder, liquid, or solid form, selecting a suitable material for specific applications can be challenging. As a result, post-processing treatments are often required to improve surface properties and ensure adequate performance.

3.1.2 AM Applications

When developing a product, both its intended application and material composition must be considered. Since multiple Additive Manufacturing (AM) techniques can be applied to the same purpose, the design process should begin by defining product requirements, followed by the selection of the most suitable fabrication method [36].

AM technologies are applied across diverse sectors, including the automotive, aerospace, medical and casting industries [36]. They are also valuable for educational applications and for preoperative planning of complex surgical procedures [41]. Owing to their computer-aided nature, AM techniques can incorporate patient-specific imaging data, enabling the customization of implants and medical devices [41].

In the biomedical field, AM has become particularly relevant within Tissue Engineering [42]. Replicating tissue architecture requires the ability to reproduce structural features at both the microscale and nanoscale. AM enables the fabrication of scaffolds with tailored porosity, geometry and shape [42], thereby supporting effective cell adhesion, proliferation and growth [38].

3.2 Electrospinning

Electrospinning, first introduced in 2001 as an AM technique [43] is based on applying a high voltage to either a polymer melt or a polymer solution, generating a charged jet that is subsequently directed toward a collector [37][44][45]. This process enables the fabrication of nanofibrous structures, a feature that is particularly attractive in the field of Tissue Engineering [43].

The technique operates through ion mobility: when an electric field is applied, the movement of ions induces surface instabilities, ultimately driving the polymer jet toward the collector. This occurs due to the electrostatic interaction between the electrical charges carried by the polymer and the applied field [46].

A conventional electrospinning apparatus typically includes a high-voltage power supply, a pump, a syringe with a nozzle and a collector plate (Figure 8). Nonetheless, variations in polymer heating and delivery methods allow for different system configurations [43]. Regardless of these modifications, the essential components - spinneret, power supply and collector - must be arranged in sequence to ensure proper operation [44].

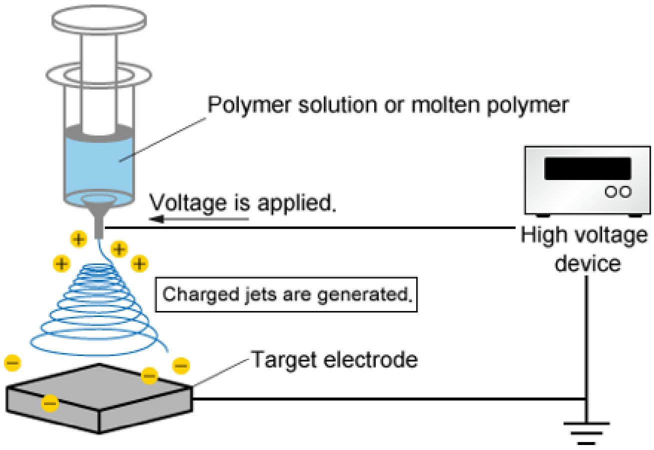

Figure 8 *Representation of the main components of an electrospinning device* [8].

In electrospinning, the polymer is delivered through a spinneret connected to a feeding system. Depending on the specific configuration, this system may consist of a syringe operated by air pressure or an extruder equipped with heating elements to melt the polymer. Such setups can accommodate single or multiple needles/nozzles, enabling controlled extrusion of the material [44].

3.2.1 Electrospinning techniques

Electrospinning can be performed using two main approaches: Solution Electrospinning (SES) and Melt Electrospinning (MES). In SES, the polymer is dissolved in a solvent to form a solution, whereas in MES, the polymer is processed in its molten state without the addition of solvents [44].

SES is the most widely employed method for producing submicron fibers. However, its reliance on solvents introduces several drawbacks: high costs, potential cytotoxicity and limited suitability for biomedical applications [44]. Furthermore, meshes fabricated through SES typically lack precise fiber deposition, requiring additional strategies to induce porosity. Without such modifications, the resulting structures may exhibit insufficient pore size for effective cell adhesion [43].

By contrast, MES avoids solvent-related cytotoxicity, making it more appropriate for biomedical use, particularly in scaffold fabrication. This method can generate fibers ranging from the microscale to nanoscale and, due to the higher viscosity of polymer melts compared to solutions, offers greater stability and deposition accuracy [44]. An advanced variation of this technique, known as MEW, integrates computer-controlled motion to enable direct writing of highly ordered fiber architectures [38].

3.2.2 Materials used in Electrospinning

Electrospinning enables the generation of nanofibers from a broad spectrum of materials, including organic polymers, self-assembling small molecules capable of forming sufficient chain entanglements, and colloidal particles [47]. Polymers, ceramics and composites can all be processed into fibers, provided that the material can either be melted or dissolved into a suitable solution. Among these options, polymers are most frequently employed, as they offer more straightforward processing and consistent fiber formation compared to other material classes [44].

PCL is one of the most widely used polymers for electrospinning in biomedical research. Its popularity stems from its biodegradability, biocompatibility and favorable mechanical properties, which together make it highly suitable for medical implants and scaffolds. PCL degrades slowly through hydrolysis of its ester linkages, ensuring prolonged mechanical support during tissue regeneration. Moreover, its relatively low melting point and excellent solubility in common solvents facilitate processing, while its flexibility and tunable mechanical strength allow adaptation to different biomedical applications. For these reasons, PCL-based electrospun fibers have been extensively investigated for tissue engineering and regenerative medicine [47].

3.2.3 Advantages of Electrospinning

Electrospinning is a relatively simple and low-cost technique that has become widely adopted in research for the fabrication of polymeric fibers [43]. Its popularity is largely due to its versatility, ease of operation and ability to process a broad range of polymers compatible with the method [44].

Compared to alternative fiber-production techniques such as wet spinning or extrusion molding, electrospinning requires fewer processing steps, making it more efficient [44]. The method also enables the blending of multiple polymers, which can be co-injected into the feeding system to produce fibers with tailored mechanical and structural properties. Furthermore, electrospinning offers flexibility in the choice of collector substrates, which may include metals, nonwoven mats, or even commercial membranes, thereby expanding its applicability across different fields [48].

3.3 Melt Electrospinning Writing

MEW is a high-resolution AM technique that integrates principles of both electrospinning and melt extrusion [37]. This approach enables the controlled deposition of fibers with diameters typically ranging from 0.005 to 0.03 mm [49].

A standard MEW system consists of a printing head, nozzle, heating unit, polymer delivery system, high-voltage power supply, computer and a movable collector [50]. In this setup, the polymer is first heated and melted within the printing head, after which it is supplied to the nozzle. An electric field established between the nozzle and the collector exerts electrostatic forces on the polymer, resulting in the formation of a Taylor cone at the nozzle tip [48][50]. The stability of this cone is essential for regulating jet diameter and ensuring steady fiber deposition. Figure 9 shows the main components of a MEW device and illustrates how the whole process works.

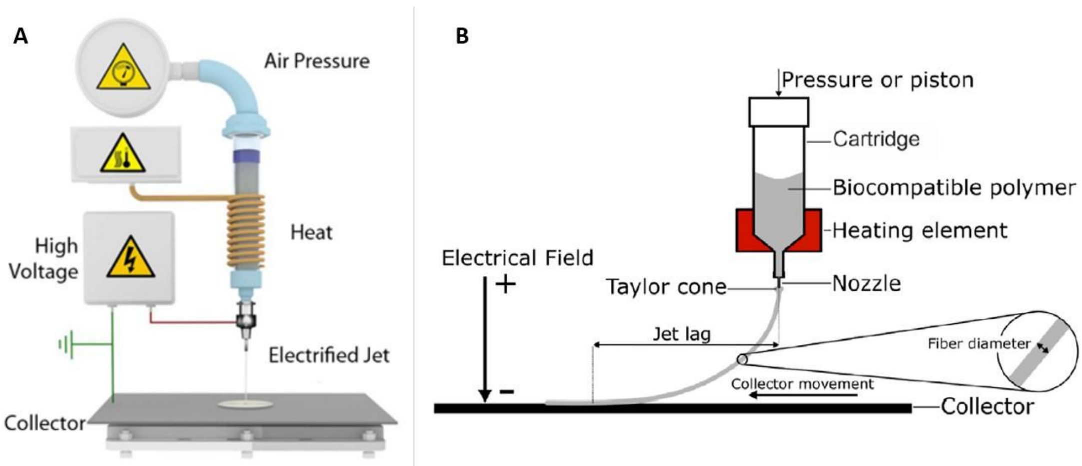

***Figure 9** Main components of a MEW device (A) and representation of MEW process (B)* [41].

For proper operation, a MEW device requires: (i) a supply zone to heat and deliver the polymer melt to the spinneret; (ii) a collection zone to receive the deposited fibers; and (iii) sufficient polymer charging to induce Taylor cone formation, enabling the polymer jet to be drawn to the collector, where it subsequently cools and solidifies [51].

When fabricating a scaffold or model, it is critical that the produced fibers match the intended diameter in order to prevent structural defects and ensure mechanical integrity [52]. Achieving this requires a thorough understanding of jet dynamics under the influence of the applied electric field, as these directly affect fiber dimensions.

Within the nozzle, the polymer becomes electrically charged, exits as a droplet and deforms into a Taylor cone. From the cone's apex, a fluid jet emerges, which is subsequently drawn toward the oppositely charged collector by electrostatic forces [48][51]. These forces not only stretch the jet, thereby reducing fiber diameter, but also enhance process stability by improving jet control [52].

Viscosity plays a central role in this mechanism, as the interplay between viscous resistance and electrostatic forces dictates the final fiber geometry. A proper balance results in uniform, thin fibers, whereas insufficient stretching leads to thicker filaments. Conversely, if electrostatic forces greatly exceed viscous resistance, the jet becomes unstable and produces irregular fibers [50].

3.3.1 Parameters

The quality of printed structures in the MEW process is influenced by a range of parameters, which can be broadly divided into material-related and process-related factors [2].

The material parameters include**:**

- **Molecular weight, melt flow rate and viscosity:** Higher molecular weight polymers exhibit greater viscosity, reducing melt flow and making extrusion more difficult. Most polymers used in MEW are therefore highly viscous. While heating can decrease viscosity and facilitate flow, excessive temperatures risk thermal degradation. Conversely, polymers with very low viscosity are unsuitable, as the jet may break under the influence of the applied electric field [53].
- **Electrical conductivity:** To preserve the stability of the electric field between the spinneret and collector, the material should exhibit low conductivity [37].

Whereas process parameters include:

- **Temperature:** During MEW, polymers are heated above their crystalline melting point to reduce viscosity, which facilitates extrusion and enables the production of thinner fibers. However, excessive temperatures can trigger thermal degradation, destabilizing the jet and compromising fiber quality [37].
- **Applied voltage:** The electric field generated by high voltage is essential for producing fibers with small diameters. Nevertheless, excessively high voltages intensify the field strength, accelerating extrusion and enlarging the Taylor cone. This leads to the formation of fibers with greater diameters instead of thinner ones [54].

- **Flow rate:** Increasing the flow rate decreases the stretching forces acting on the jet, resulting in thicker fibers. Conversely, reducing the flow promotes smaller diameters, but excessively low flow rates hinder the stable formation of the Taylor cone [53].
- **Collector speed:** The translation speed of the collector strongly influences fiber morphology. When the collector operates above the critical speed, straight fibers are obtained; below this threshold, curled fibers are produced. Nonetheless, overly high speeds can compromise precision during deposition [55].
- **Tip-to-collector distance:** A greater separation reduces the electric field strength, generally leading to thinner fibers. However, longer travel distances allow the jet to solidify prematurely, weakening fiber adhesion and negatively affecting the stability of the 3D structure [53].

3.3.2 Advantages of Melt Electrospinning Writing

Although fewer than 1% of publications on electrospinning techniques specifically address MEW, the method presents several notable advantages. One of its key benefits is the high degree of customizability: research groups can design and assemble their own MEW systems tailored to experimental needs, often at a lower cost than conventional filament fabrication equipment [51].

MEW produces a continuous and stable polymer jet by applying high voltage between the nozzle and the moving collector [53]. The resulting melt jet exhibits enhanced stability, which allows predictable and precise fiber deposition. This makes it possible to fabricate highly ordered structures, such as scaffolds with controlled pore size and defined geometries [50]. Additionally, MEW can generate fibers with smaller diameters than those typically produced by SES [53].

The incorporation of moving collectors further improves deposition accuracy and enables the fabrication of layer-by-layer architectures with tailored shapes and designs [54]. Compared to SES, MEW offers superior control over fiber placement, yielding structures that more closely match the intended design in terms of shape, volume and overall architecture [51].

Unlike Solution Electrospinning (SES), Melt Electrospinning Writing (MEW) is a solvent-free technique, which enhances its biocompatibility and broadens its potential applications in the medical field [56]. MEW-generated scaffolds exhibit controlled porosity, enabling efficient cell attachment, proliferation and extracellular matrix formation through rapid and uniform cell infiltration [49].

This approach is particularly well suited for thermoplastic processing, making it possible to employ biocompatible polymers [6]. Under appropriate conditions, specifically, high viscosity and low electrical conductivity, the melt forms a stable, straight jet that solidifies precisely upon deposition. The absence of residual solvent additionally allows for reliable layer-by-layer fabrication, facilitating the construction of well-defined three-dimensional architectures [49].

3.3.3 Use of MEW for POP Repair

MEW enables the processing of various biocompatible and biodegradable polymers, making it a promising tool for multiple applications in Tissue Engineering [38]. However, research specifically focused on the development of MEW-fabricated biodegradable meshes for POP repair remains limited [57].

Ren et al. [57] investigated the potential of MEW-produced composite meshes for POP treatment by employing two FDA-approved biodegradable polymers: PCL and polyethylene glycol (PEG). Their study examined how material selection, mesh geometry (achieved by varying filament spacing), and mesh condition influenced performance. To evaluate these factors, the researchers conducted tensile and degradation tests, as well as antimicrobial, antibiotic and biocompatibility assessments.

The study concluded that composite PCL–PEG meshes degrade more rapidly than pure PCL scaffolds, suggesting that by adjusting the PCL:PEG ratio, it is possible to tailor the degradation profile to match the rate of pelvic tissue regeneration. Under physiological conditions, higher PEG content was associated with increased mass loss. From a mechanical perspective, the composite meshes demonstrated greater strength than scaffolds containing only PCL. Similarly, stiffness increased with PEG content, whereas variations in mesh geometry (1.0 mm vs. 1.5 mm filament spacing) had no significant influence on tensile strength [57].

Given that polypropylene (PP) meshes are associated with elevated risks of infection and inflammation, the authors also incorporated antibiotics into the composite scaffolds and evaluated different dosages [57]. Their findings indicate that MEW can be used to fabricate biodegradable meshes with tunable mechanical properties, controlled degradation and the capacity for antibacterial functionality through slow drug release. Such meshes represent a promising alternative to PP-based implants for POP treatment, eliminating the complications associated with synthetic permanent materials.

3.4 Auxetic Structures

Auxetic structures are widely recognized for their remarkable properties, including high toughness, resilience and shear resistance. Beyond these characteristics, they possess a distinctive feature that sets them apart from conventional materials. While traditional materials generally become thinner when subjected to tensile loading, auxetic structures exhibit the unusual ability to expand laterally and become thicker under the same conditions. Figure 10 illustrates the difference in behaviour between conventional materials and auxetic materials

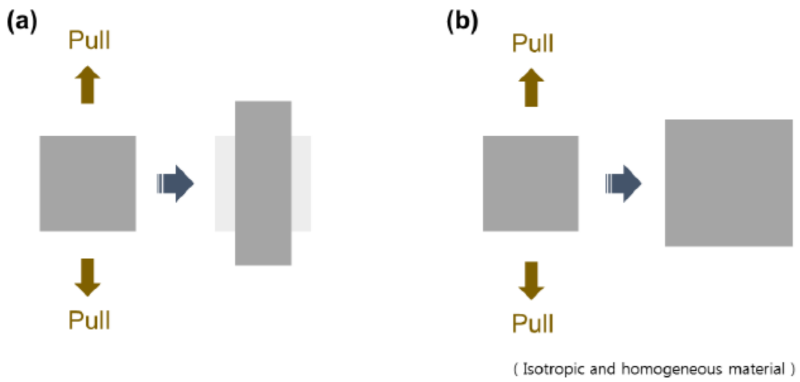

Figure 10 *Behaviours of (a) conventional material and (b) auxetic (negative Poisson's ratio) material* [58].

The defining parameter of this auxetic behavior is Poisson's ratio, which measures the deformation of a material in the transverse direction relative to its deformation in the axial direction when an external force is applied. In other words, it represents the ratio between transverse (ε_y) and axial (ε_x) strains and is calculated using the following Equation (3.1):

$$v_{xy} = -\frac{\varepsilon_y}{\varepsilon_x} \tag{3.1}$$

Most materials contract laterally under longitudinal tensile forces, yielding a positive Poisson's ratio. For this reason, the negative sign is introduced in the formula to ensure that the values of Poisson's ratio for conventional materials remain positive. However, in auxetic materials, Poisson's ratio takes on negative values, as these structures expand laterally when stretched (or contract laterally when compressed). This distinctive mechanical response has attracted growing interest, particularly in biomedical applications, since it mimics certain behaviours observed in biological tissues, which often exhibit negative Poisson's ratios [58] [59].

Currently, auxetic frameworks are categorized into different classes according to the way the auxetic effect is produced or by the design principles of their structural components. Examples include foldable structures, nodular and fibrillar frameworks. Up to the present, several types of auxetic structures have been investigated to induce the auxetic effect. The terms *re-entrant* [59], *chiral* [60] and *rotating* [61] have been employed to classify these structures according to the specific mechanisms responsible for producing the auxetic behaviour.

3.4.1 Re-entrant Unit Cells

Re-entrant structures are highly anisotropic, a property that is essential to auxetic behavior. As implied by their name, these geometries consist of ribs forming the unit cell that bend inward. Figure 11 illustrates different types of re-entrant structures, highlighting their defining unit cells. The inwardly angled ribs of these cells are directly responsible for the auxetic response, enabling the structure to expand in both longitudinal and transverse directions when subjected to tensile loading.

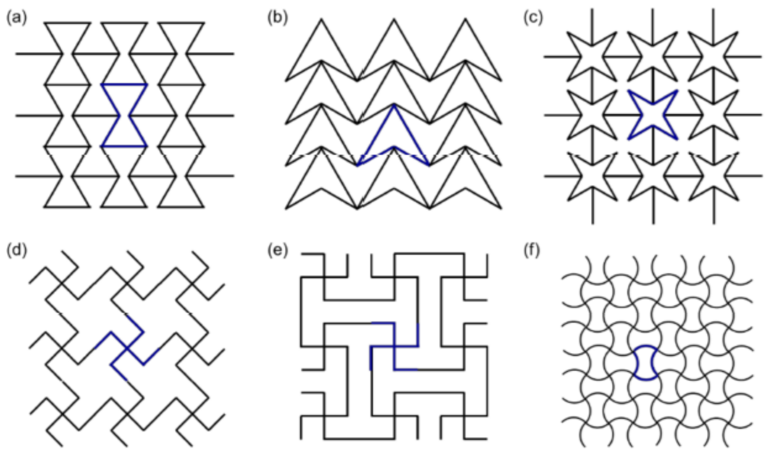

Figure 11 *(a)Re-entrant honeycomb,(b)double arrowhead,(c)star honeycomb,(d)structurally hexagonal re-entrant honeycomb,(e)lozege grids,(f)sinusoidal ligaments* [62].

For instance, in the first structure depicted in Figure 11, applying a tensile force along the horizontal axis causes the diagonal ribs to rotate vertically. This internal rotation mechanism drives expansion in the transverse direction, thus generating the auxetic effect [62].

Auxetic behavior is also observed in other re-entrant configurations. As illustrated in Figure 11 (b) and (c), the auxetic response in the double-arrowhead structure arises from the displacement of the arrowheads, while in the star honeycomb it results from rib flexure and hinging mechanisms [63][64]. Additional re-entrant geometries were obtained by introducing hinging along the side edges of lozenge and square grid patterns (Figure 11(d) and (e)) where the bold-marked regions represent the unit cells [65][66]. In these cases, the auxetic effect originates from the combined expansion and rotation of the structural lines forming the unit cells. Another example is the quilted structure incorporating sinusoidal ligaments (Figure 11(f)) in which the auxetic response is governed by the stretching of the sinusoidal curves. Moreover, these sinusoidal ligaments may be substituted by hinged linear ligaments, enabling structural variation [67].

It is important to note that in this study, the auxetic geometries that were studied belong to this group, i.e., re-entrant structures, more specifically the re-entrant honeycomb design and the double arrowhead design.

3.4.2 Chiral Unit Cells

Chiral auxetic structures, on the other hand, consist of straight ribs tangentially attached to the outer surface of central nodes. These nodes may be circular or take the form of other closed-loop geometries, as shown in Figure 12.

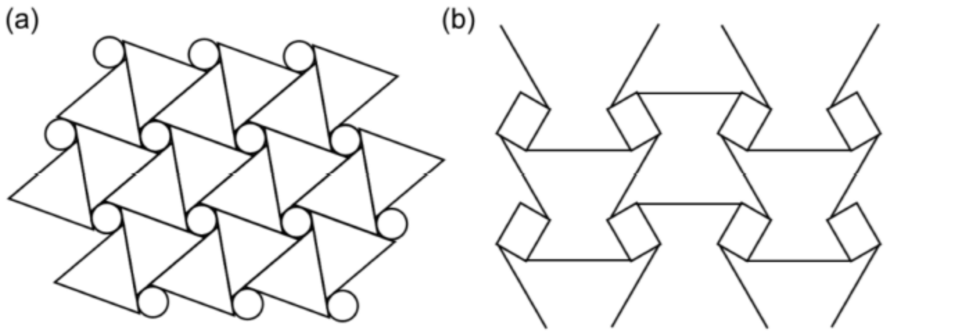

Figure 12 *Chiral structures.(a)chiral structure with same units,(b)chiral structure with symmetrical units* [62].

When subjected to an external load, chiral auxetic structures transfer the applied force through their ligaments toward the central nodes [68]. This generates torque on the nodes, and their subsequent rotation transmits the force to the surrounding ribs. The auxetic effect arises from the wrapping or unwrapping motion of the ribs driven by this nodal rotation.

These configurations typically exhibit high porosity, which contributes to their lightweight nature but often compromises durability and structural stability [69]. Unlike other auxetic designs, chiral unit cells usually lack symmetry lines, further influencing their anisotropic response.

3.4.3 Rotating Unit Cells

Rotating unit cells are designed to induce auxetic behavior in networked polymers and foams at both the microscale and nanoscale. These frameworks rely on rigid or semi-rigid polygons, such as triangles and rectangles, connected at selected vertices by hinges or elastic joints [61]. When subjected to tensile forces, the relative rotation of these polygons produces the auxetic effect (Figure 13).

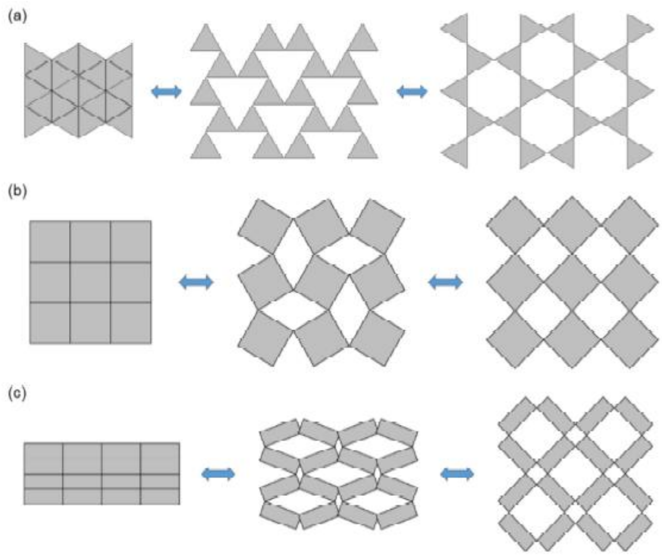

Figure 13 *Rotating unit structures. (a) Triangle unit cells, (b) square unit cells, (c) rectangle unit cells* [58][61][70][71].

The underlying mechanism is related to the initial orientation of the rigid units. Because the applied load is not collinear with the alignment of the top and bottom vertices, torque is generated in each unit cell. This torque induces the rigid polygons to rotate alternately in opposite directions, either clockwise or counterclockwise, relative to their neighbors. As the units themselves do not deform, the hinges absorb the resulting strain [72].

This rotational motion drives the transverse displacement of the semi-rigid hinges, expanding the framework in the perpendicular direction to the applied load and generating the auxetic effect. The process continues until all rigid units align with the tensile axis, at which point the structure reaches its maximum expansion, as illustrated in Figure 13.

3.4.4 Fabrication of the Auxetic Structures

AM

Additive manufacturing represents the most versatile approach for producing auxetic architectures, as it provides precise control over geometry, porosity and fiber orientation [73]. Techniques such as fused deposition modeling (FDM), stereolithography (SLA/DLP), selective laser sintering (SLS) and MEW allow the fabrication of complex 3D constructs with tailored mechanical properties [74]. These methods facilitate the development of patient-specific scaffolds and the integration of multiple biomaterials [75]. Despite these advantages, AM processes remain relatively costly and time-intensive compared to conventional fabrication routes [76].

Soft Lithography

Soft lithography enables the patterning of microscale and nanoscale auxetic features through molding or stamping processes that employ elastomeric templates [77]. This technique achieves a high degree of accuracy at small scales, making it particularly suitable for biomedical microdevices, such as stents or implantable membranes. However, its scalability to clinically relevant dimensions is limited and the associated fabrication costs are considerable [78].

Machining-Based Technologies (fabrication using machining technology)

Auxetic patterns can also be generated through machining methods, including laser cutting, waterjet cutting or micromachining of polymeric, metallic, or composite sheets. These processes are efficient for rapid prototyping and for producing two-dimensional or quasi-two-dimensional auxetic designs. Nevertheless, their applicability to highly complex three-dimensional geometries is restricted, which can limit their utility in advanced biomedical applications [79].

Compressed Foams

Conventional open-cell foams, such as polyurethane, may be converted into auxetic structures through mechanical compression followed by thermal treatment, leading to re-entrant cell morphologies [65]. The main advantages of this approach are its low cost, simplicity and scalability. On the other hand, the method provides limited control over pore geometry and mechanical performance, which reduces its suitability for applications that demand high precision [80].

Textile Technologies

Textile-based methods, including specialized weaving, knitting and braiding patterns, can impart auxetic behavior to fabrics and fiber assemblies [81]. These structures are lightweight, flexible and capable of conforming to soft tissues, making them attractive for biomedical applications such as patches, prosthetic reinforcements, and wearable devices [82]. Their limitation lies in the difficulty of achieving well-defined and reproducible three-dimensional auxetic architectures [83].

3.4.5 Prospect of the Auxetic Structures

In fact, auxetic structures, exhibiting a negative Poisson's ratio, offer significant potential for biomedical applications due to their distinctive mechanical behavior. A wide range of materials has been explored for their fabrication, including natural and synthetic polymers, composites, ceramics, foams and textiles. Various manufacturing techniques have been employed to generate these architectures, ranging from additive manufacturing and soft lithography to machining, compressed foams and textile-based approaches [84]. Each technique provides distinct advantages in terms of precision, scalability and achievable geometries, which in turn influence the mechanical response of the resulting constructs [85].

Firstly, auxetic geometries can distribute mechanical loads more uniformly, thereby reducing localized stress concentrations that often contribute to implant failure or tissue erosion in conventional meshes. Their ability to conform closely to surrounding tissues also enhances implant integration and comfort, minimizing the risks of mechanical mismatch. In addition, the lateral expansion under tensile loading naturally increases pore size, facilitating improved cell infiltration, vascularization, and tissue ingrowth, critical factors for long-term biocompatibility and functional repair.

The integration of auxetic designs into biodegradable meshes represents a novel approach to addressing the shortcomings of conventional polypropylene-based implants. By combining mechanical adaptability, enhanced tissue compatibility, and favorable biological performance, auxetic meshes hold the potential to offer safer and more effective alternatives for POP treatment.

In vitro studies consistently report that auxetic scaffolds display favorable performance in terms of cellular compatibility, proliferation and differentiation, suggesting that their unusual deformation mechanisms may create more physiologically relevant mechanical environments compared to conventional, non-auxetic designs [86]. Moreover, their adaptability under strain and ability to distribute stresses more evenly make them highly attractive for biomedical devices such as stents, implants, prosthetic reinforcements and tissue engineering scaffolds [87].

These conclusions align closely with the thematic focus of the present dissertation. The use of auxetic meshes as implantable scaffolds for the treatment of pelvic organ prolapse (POP) leverages precisely these advantages. POP repair requires materials that combine sufficient mechanical support with compliance similar to that of vaginal tissue, while avoiding the complications associated with conventional synthetic meshes, such as excessive stiffness, erosion and rejection. Auxetic meshes, by virtue of their geometry-driven deformation, have the potential to provide superior load distribution, reduce localized stress concentrations and better mimic the mechanical behavior of the native pelvic floor.

In addition to comparing biodegradable meshes with auxetic designs to synthetic meshes, these meshes can also be compared to biodegradable meshes with regular, i.e. non-auxetic, designs. Biodegradable meshes with regular non-auxetic designs, such as square-shaped mesh (orthogonal grid) and diagonal-shaped mesh (lozenge mesh), exhibit predictable mechanical behaviour, with greater initial stiffness and lower deformation capacity before failure. This type of architecture tends to concentrate localized stresses under multiaxial loads, resulting in more sudden failure, which contrasts with the anisotropic and highly deformable behaviour of native vaginal tissue [2][57]. In contrast, auxetic designs, such as re-entrant honeycomb and double arrowhead, are characterized by a negative Poisson's ratio: they expand transversely when subjected to traction, which gives them reduced initial stiffness, followed by greater deformability, higher energy absorption and uniform stress distribution in uniaxial and ball burst tests [88][89].

Thus, the conclusions of the literature on auxetic structures reinforce the idea of investigating and mechanically characterizing meshes with auxetic design in the context of POP repair, as carried out in this study, in which two biodegradable auxetic PCL (re-entrant honeycomb and double arrowhead) printed by Melt Electrospinning Writing are studied.

Chapter 4

Materials and Methods

4.1 Materials

4.1.1. Technical PCL

Polycaprolactone (PCL), a polymer approved by the FDA, has become one of the most widely investigated materials for additive manufacturing, particularly in MEW. Its popularity arises from its advantageous processing properties, including a relatively low melting temperature and rapid solidification, which make it highly suitable for precise fiber deposition [32]. Belonging to the poly-α-hydroxy acid family together with polylactic acid (PLA) and polyglycolic acid (PGA), PCL is a biodegradable and biocompatible material. It was first synthesized in the early 1930s through the ring-opening polymerization of ε-caprolactone [90].

This semi-crystalline and hydrophobic polymer presents a glass transition temperature of approximately -60 °C and a melting point in the range of 59-64 °C. Compared to other degradable polymers, PCL exhibits superior viscoelastic behavior, which simplifies processing and enables the fabrication of complex and diverse structures [90].

Owing to its favorable properties, PCL has been widely applied in biomedical contexts, including the production of resorbable sutures, drug delivery systems and scaffolds for tissue engineering. Its slow rate of hydrolytic degradation makes it suitable for long-term applications, while its proven ability to promote cell adhesion and proliferation further reinforces its biomedical relevance [91].

For the present work, the biodegradable meshes were manufactured using technical-grade PCL provided by Filament-PM and the version used was $Facilan^{TM}$ PCL 100, which has a filament diameter of 1.75 mm, a density of 1.1 g/cm³ (ISO 1183), a melting point of 58-60°C and a decomposition temperature of 200°C. Regarding mechanical properties, the PCL fiber has a tensile strength of 45MPa, a tensile modulus of 350 MPa and an elongation at yield of 15% [92]. During printing, both temperature and humidity were controlled to guarantee reproducibility and quality of the produced scaffolds.

4.1.2 Sow´s Tissue

Although the use of animals in biomechanical research can be traced back to ancient Greece, their systematic application in injury biomechanics only became established during the mid-20th century. Due to the ethical and practical restrictions of exposing human subjects to sub-injury threshold testing, animal models provide the most feasible alternative for examining the pathophysiological responses to impact and for understanding the subsequent consequences of such injuries.

Over the past decade, several studies have emphasized the suitability of pigs as experimental models for biomedical research. Despite their distinct external morphology, pigs share extensive biological and physiological similarities with humans, making them among the closest animal models available for translational studies, with only a few exceptions [4]. Pigs have significant benefits over primates and other livestock models due to their greater litter sizes, shorter generation periods and easily manipulable genomes [4].

In the context of this work, approval for the collection of sow vaginal tissues was obtained from the Direção-Geral da Alimentação e Veterinária (DGAV), Porto, Portugal (protocol: N19128UDER). The tissues were harvested at the Euroabate – Matadouro Industrial, Lda (NCV D 42), located in Marco de Canaveses, Portugal. For the ball burst tests, the vaginal tissue sample measured approximately 50 mm in width, 50 mm in length and 4 mm in thickness (Figure 14). The dimensions of the biological sample for the uniaxial tests were 10 mm in width and 4 mm in thickness (Figure 15).

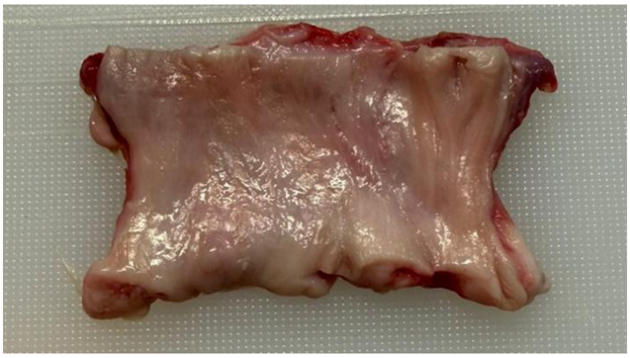

Figure 14 *Vaginal tissue sample for ball burst testing.*

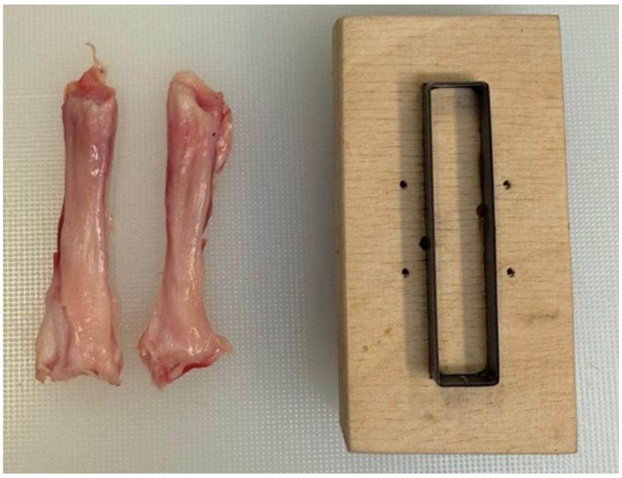

Figure 15 *Vaginal tissue sample for uniaxial testing.*

4.2 Instruments and Tools

4.2.1 Mesh Production

G-Code Design Software

Geometric Code (G-Code) is the standardized programming language employed in Computer Numerical Control (CNC) systems. It enables the automation of motion, precision, and process control by being directly integrated into the machine's operating software. Through G-Code, the trajectory, velocity and tool path of the machine are explicitly defined, thereby dictating its operational behavior. In the context of additive manufacturing, such as three-dimensional (3D) printing, G-Code provides the sequential instructions required for the deposition of material in a layer-by-layer fashion, ultimately resulting in the fabrication of an object with a predetermined and highly accurate geometric configuration [8]. The standard structure of a G-Code line is:

$$\boldsymbol{G}\#\# \ \boldsymbol{X}\#\# \ \boldsymbol{Y}\#\# \ \boldsymbol{Z}\#\# \ \boldsymbol{F}\#\#$$

The initial component of this structure is the G-Code Command (G). The second portion specifies the coordinates (X, Y, Z) for the machine to travel. The third section determines the feed rate (F) or movement speed.

The meshes were designed using *FullControl GCode Designer*, which generated the G-code required for the MEW prototype. The software incorporates predefined geometric functions, such as straight lines and circular paths. For mesh design, the user is required to specify the initial and final coordinates of each programmed movement (e.g., in the case of a Cartesian line), as well as the extrusion parameters and the corresponding movement speed. Furthermore, the system allows the selection between "Print" and "Travel" commands, thereby distinguishing movements associated with material deposition from those performed without extrusion. In addition, the user can configure various process parameters, including printing temperature, to ensure appropriate fabrication conditions.

To verify the accuracy of the designs prior to printing, the generated G-code was visualized using NC Viewer, allowing a preview of the mesh structures.

Melt Electrospinning Writing Prototype

The PCL meshes were fabricated using a MEW prototype, developed in 2021 within the scope of the *SPINMESH* project. The device is composed of several main components, including the structural frame, linear actuators, collector plate, extruders, a graphical touchscreen interface, and a high-voltage generator, as shown in Figure 16. Figure 17 shows the MEW prototype's touchscreen graphical user interface, which aids in its operation. Although the system supports multiple extrusion options, only the filament extruder was employed in this study.

Movement precision is a key requirement in MEW, and in this prototype, it is achieved through Cartesian configuration. The collector is driven by linear actuators, enabling displacement along the X and Y axes, while vertical motion (Z axis) is provided by the print head, with a maximum build height of 70 mm. The spinneret is a conventional fused filament fabrication (FFF) nozzle, at whose tip the Taylor cone is formed. The nozzle orifice measures 0.4 mm, which also defines the upper limit of fiber diameter.

The high-voltage source, as shown in Figure 18, delivers up to 60 kV with 150 W of power and a minimum output current of 0.01 mA. The collector consists of a 270 × 270 mm^2 square aluminum plate with a thickness of 3 mm, selected for its high electrical conductivity. The prototype is housed at the Product and Services Development Laboratory (LDPS), Faculty of Engineering of the University of Porto (FEUP).

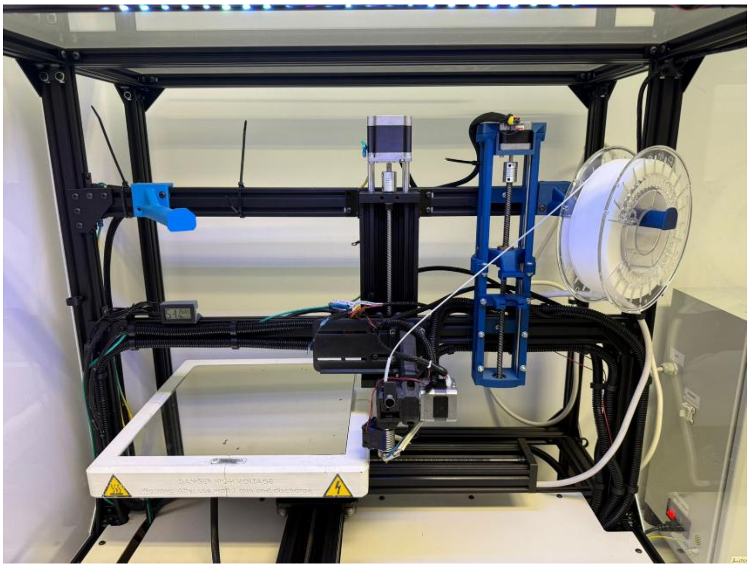

Figure 16 *Melt electrowriting device.*

Figure 17 *Graphical touchscreen interface of the MEW prototype.*

Figure 18 *High-voltage generator (voltage source).*

Optical Characterization

The morphology and quality of the printed meshes were assessed using a *Leica Emspira 3* digital microscope (Leica Microsystems, Wetzlar, Germany). This equipment allows high-resolution optical imaging and real-time visualization without the need for eyepieces, providing precise surface inspection of samples. The microscope is equipped with an integrated LED illumination system and a digital camera that enables image capture and documentation directly through its user interface.

The *Emspira 3* supports variable magnification through adjustable objective lenses and fine focusing, which permits accurate evaluation of fiber orientation, pore size and mesh geometry. Images obtained with this device were used to qualitatively confirm the reproducibility of the printing process and to detect possible defects in the manufactured scaffolds. Figure 19 shows the digital microscope used in this study.

Figure 19 *Digital microscope (Leica Microsystems, Wetzlar, Germany).*

4.2.2 Mechanical Tests

The mechanical properties of the printed filaments were evaluated through uniaxial tensile tests using a *Mecmesin Multitest 2.5-dV* testing machine, equipped with a Mecmesin Advanced Force Gauge (AFG) load cell with a capacity of 100 N (as it provides more accurate results than a 2500 N load cell). The tests were performed at a constant crosshead speed of 10 mm/min, and data acquisition was managed with *VectorPro Lite software* which, when connected to the load cell, allows all measured data to be collected (load applied to the mesh, as well as the displacement of the folds).

To carry out the ball burst tests, the system consists of a cylindrical indenter 55 mm long and 11.5 mm in diameter, attached to a clamping fixture containing a circular opening 20 mm in diameter, designed to hold and secure the specimen during the test. During the test, the indenter was moved vertically at a constant speed of 10 mm/min, applying a progressively increasing compressive load until failure of the mesh, the fabric or the fabric-mesh system occurred. The test speed was selected to ensure quasi-static loading conditions, minimizing dynamic effects and ensuring stable contact between the indenter and the specimen. Furthermore, this speed was kept consistent with that used in the uniaxial tests carried out in this study, allowing for a more direct comparison between the different methods of mechanical characterization. During the test, the indenter load and displacement values were continuously recorded until failure occurred or the specimen’s load-bearing capacity was significantly reduced.

In addition to filament testing, both uniaxial tensile and ball burst tests were performed on the vaginal tissue samples and the printed meshes using a *Mecmesin Multitest 2.5-dV.* For the uniaxial tests, a 100 N load cell was employed with a constant elongation rate of 10 mm/min. For the ball burst tests, the crosshead speed was set to 10 mm/min in compression mode and the load cell for de meshes was a 100 N load cell but for the tissue it was used the 2500 N load cell. Figures 20 and 21 show the apparatus used for uniaxial mechanical testing and ball burst testing, respectively.

Figure 20 *Uniaxial tensile test machine used to perform uniaxial tensile tests.*

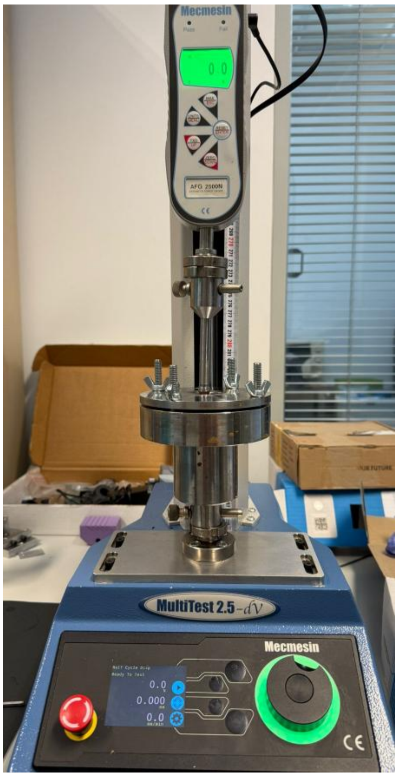

Figure 21 *Ball burst machine used to perform ball burst tests.*

These experiments provided critical information on the mechanical response of both the biological tissue and the manufactured meshes, offering a comparative assessment of their performance under controlled loading conditions.

4.3 Mesh Prototyping

To establish the desirable characteristics of meshes for POP repair, it is essential to examine both currently available designs and those historically applied in clinical practice. Literature reports indicate that an optimal mesh thickness typically falls within the range of 0.08 mm, 0.16 mm, and 0.24 mm, while pore sizes of approximately 2.0 mm are considered advantageous for promoting cell ingrowth and supporting tissue integration in prolapse correction. The re-entrant honeycomb design is widely studied due to its simple geometry and pronounced auxetic effect, offering improved flexibility and energy absorption. The double arrowhead pattern, on the other hand, provides higher stiffness and strength while maintaining auxetic properties, making it particularly promising for load-bearing applications [58].

In this dissertation, the focus is placed on meshes with a pore size of 3.0 mm and a thickness of 0.24 mm. Furthermore, two distinct auxetic geometries were selected for investigation: the double arrowhead and the re-entrant honeycomb structures, given that, based on the work carried out in the laboratory, it was concluded that these two geometries showed the greatest potential. These configurations are of particular interest due to their potential to provide enhanced mechanical performance and favorable biological responses compared to conventional mesh designs.

Auxetic structures expand laterally when stretched and contract when compressed, which is the inverse behavior of conventional materials. This unique mechanical response provides several advantages for biomedical applications, particularly in the context of POP repair.

4.3.1 Geometry Conception

The design of surgical meshes for MEW requires translating conceptual geometries into machine-readable code. Unlike conventional manufacturing methods, AM enables the production of multilayered meshes with firmly interconnected fibers, allowing greater control over thickness and the creation of structures that mimic the three-dimensional nature of biological tissues.

For this work, customized *G-code* was generated to define the mesh geometries and control the movements of the MEW device. The designs were visualized in *NC Viewer*, which facilitated real-time inspection and adjustment of the geometry. To assist in G-code creation, the open-source *FullControl* software was employed. This tool allows the generation of function-based print paths that would otherwise be impractical to develop manually, while also providing automatic calculations of filament usage and enabling precise control of geometric accuracy. The *FullControl* software allows the entrance of several parameters, such as pore size, fiber diameter, mesh size, extrusion temperature, print speed and mesh geometry.

The square configuration was selected due to its resemblance to commercially available meshes [2], while the fiber diameter values were defined in accordance with previous studies [32]. The pore size was chosen within the range considered favorable for tissue integration, as larger pores are associated with improved cell infiltration, neovascularization, and extracellular matrix deposition, thereby enhancing the biological performance of the implant.

The fiber diameter is proportional to the extrusion rate specified in the G-code. This rate refers to the amount of material extruded to produce fibers with a specific diameter. The extrusion rate is computed using the Equation 4.1:

$$E = \frac{(D_{Fiber} \times 0.001 \times 1.5)^2 \times l_{Fiber}}{D_{Filament}^2} \tag{4.1}$$

Where:

D_{Fiber} – Fiber diameter of 240 μm;

l_{Fiber} – Length of the printed mesh;

$D_{Filament}$ – Filament diameter of 1.75 mm.

So, in the equation described above, the D_{Fiber} represents the desired fiber diameter in micrometres (μm). A conversion factor of 0.001 is applied to transform measurements from micrometres to millimetres. The variable l_{Fiber} denotes the total length of the filament path as defined by the custom-generated G-code for each specific printed geometry, which can vary based on the geometric design and mesh dimensions. Moreover, the factor of 1.5 serves as a calibration factor that has been empirically determined from preliminary experiments. Finally, $D_{Filament}$ refers to the diameter of the PCL filament and its value is 1.75 mm.

It is important to note that this study did not aim to perform a parametric evaluation of fiber diameter or pore size, but rather to assess the differences in performance between two auxetic designs. However, it is important to understand the pore size in both designs studied in this paper; Figure 22 shows a schematic representation of this.

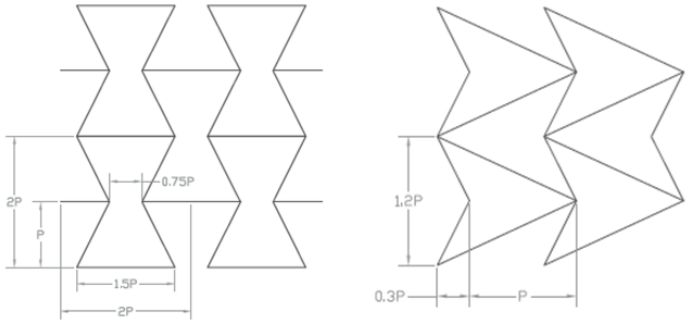

Figure 22 *Schematic representation of the pore size (P) of the two auxetic geometries, re-entrant honeycomb (left) and double arrowhead (right).*

To ensure that the meshes were printed with the intended dimensions, the printing parameters of the MEW prototype were carefully adjusted. The adjusted values of the process parameters used in the MEW prototype for printing were as follows: bed temperature at 30°C for the double arrowhead mesh, while for the re-entrant honeycomb design the temperature was 35°C; the voltage applied for the arrowhead design was 4.80 kV, while for the re-entrant design the voltage was 4.40 kV; the extruder temperature was 200°C, a 1000 mm/min printing speed had to be adjusted for the design of these geometries, i.e. a lower value compared to simple square meshes, for example, and the height between the nozzle and the bed was 2 mm, which were the same for both meshes. As regards the different applied voltage values in the two meshes tested, this difference is related to the geometry of each design itself, as it was with these voltage values that the correct shape of each mesh was achieved.

The viscosity of the material is strongly dependent on the printing temperature. At lower temperatures, specifically 160 °C and 180 °C, the viscosity remains excessively high, which hinders continuous extrusion. Conversely, at elevated temperatures of 200 °C and 220 °C, the viscosity is substantially reduced. To avoid excessively low viscosity values while still ensuring adequate processability, a printing temperature of 200 °C was selected. The voltage applied will determine the material extrusion. If the voltage is too low, it will create a weak electric field that will not be able to extrude all the material, leading to material accumulation. If the voltage is too high, the electrical field will have such high intensity that it will increase the extrusion speed, leading to points of discontinuity and instability.

The selected settings produced fiber diameters and pore sizes that closely matched the target values, which were subsequently verified using optical microscopy. These parameters enabled the deposition of a stable and continuous filament without significant elongation and with only minor deviations. All parameters were predefined within the G-code files, with the exception of the applied voltage, which was manually set through the voltage supply.

4.3.2 Printing Production

Upon finalizing the printing parameters and generating the requisite G-code, the production of meshes with dimensions of 240 micrometers and a pore size of 3 mm, featuring both with re-entrant honeycomb design and double arrowhead pattern, becomes achievable. With the meshes completed and validated, we can go on to the next step of this project, which entails determining the mechanical characteristics of both the fibers and the sow's vaginal tissue. Figures 23 and 24 show the printed meshes for each of the auxetic geometries, whilst Figures 25 and 26 illustrate the same meshes as viewed under a digital microscope.

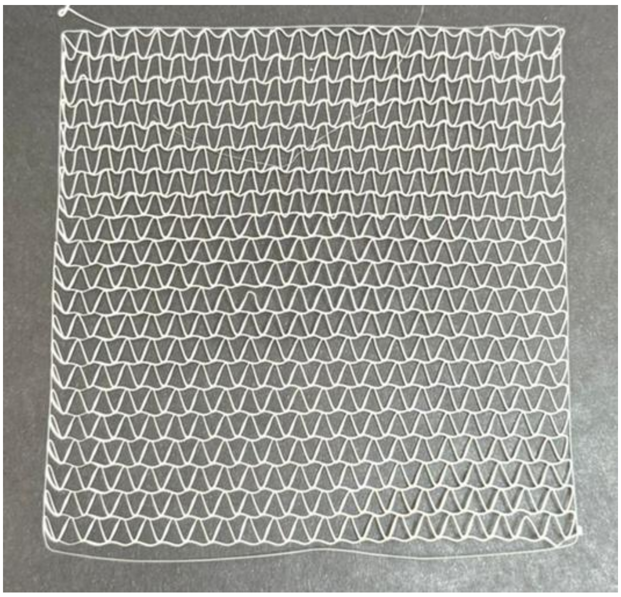

Figure 23 *Double Arrowhead design printed mesh.*

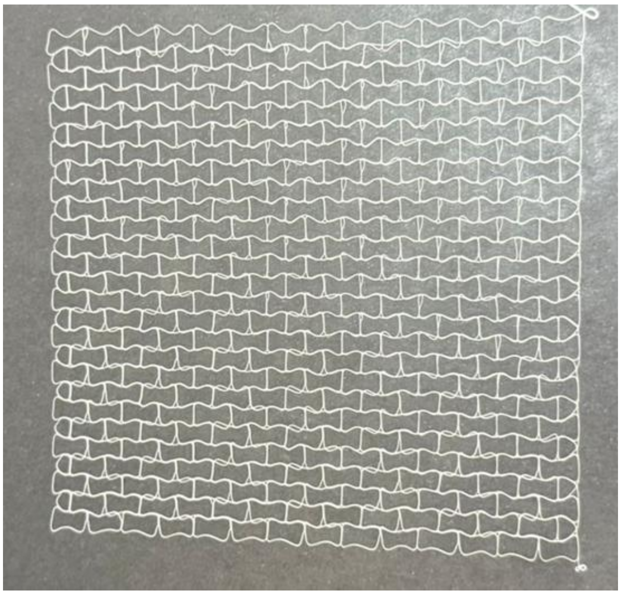

Figure 24 *Re-entrant honeycomb design printed mesh.*

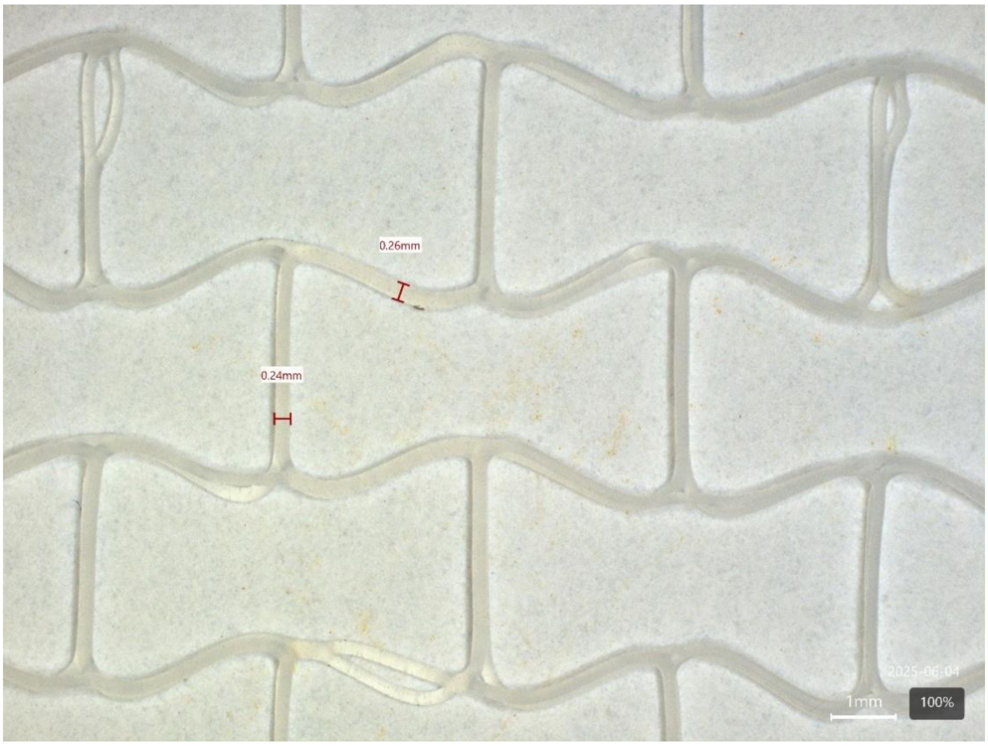

Figure 25 *Photograph of the digital microscope view of the re-entrant honeycomb mesh.*

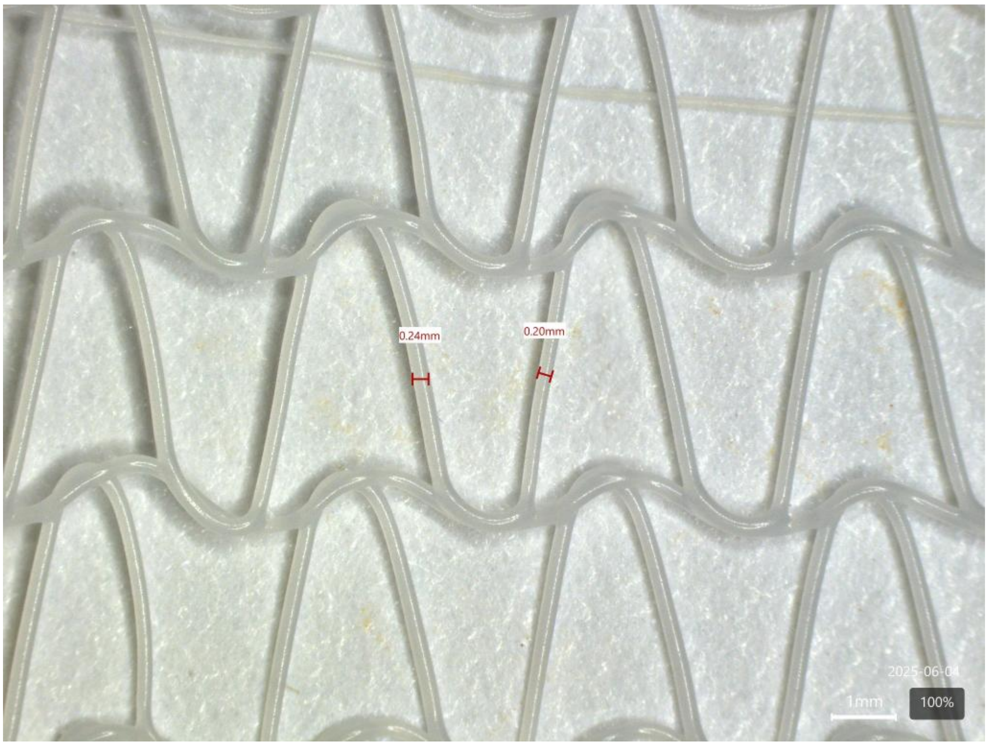

Figure 26 *Photograph of the digital microscope view of the double arrowhead mesh*

4.4 Mechanical Tests

4.4.1 Uniaxial Tensile Test

Tensile tests are an important technique for researching mechanical characteristics because they allow us to see how materials react under tension load. In this sort of test, the material is subjected to stress to determine how strong it is and how far it can be stretched before it ruptures [8]. By continuously recording the applied force and the corresponding displacement, key mechanical properties can be determined. From these measurements, parameters such as ultimate strength, stress, strain and Young's modulus are derived, providing insight into the stiffness and elasticity of the material.

In this study, uniaxial tests were performed on both sow vaginal tissue and PCL auxetic meshes to evaluate and compare their mechanical performance. The dimensions of the vaginal tissue samples were width of 10 mm and a length of 40 mm (Figure 27), as well as the cuts of the printed meshes evaluated. It is important to note that the three tissue samples were taken from the middle region of the vaginal wall. Figures 28, 29 and 30 illustrate the uniaxial test to which the double arrowhead mesh, the re-entrant honeycomb mesh and the vaginal mesh were subjected, respectively.

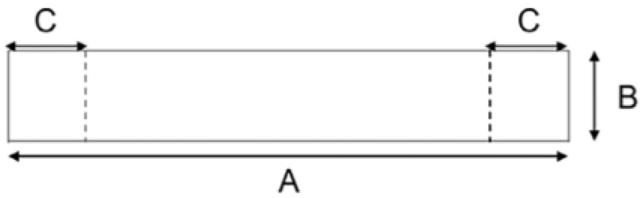

Figure 27 *Standardized dimensions for uniaxial tensile tests include a length of 40 mm (a), a width of 10 mm (b), and a fixation area (c)*

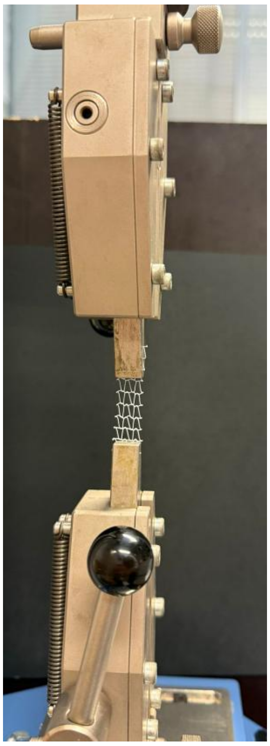

Figure 28 *Uniaxial stress test of the Double arrowhead mesh.*

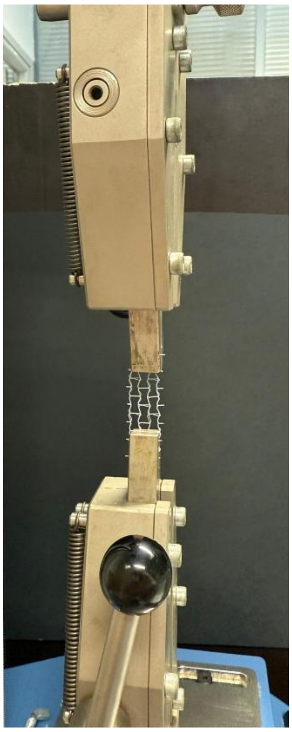

Figure 29 *Uniaxial stress test of the Re-entrant honeycomb mesh.*

Figure 30 *Uniaxial stress test of the vaginal tissue.*

Stress-strain curves are the average of three tests performed in each mesh and tissue. The assessments were conducted using the "*Mecmesin Multitest 2.5-dv*" for fiber testing and for tissue testing. Both used a 100 N load and a constant elongation rate of 10 mm/min. The samples of the meshes were placed on the equipment and the distance between the mechanical folds was also measured. Force-displacement curves were acquired for three samples of each category, which allowed obtaining average stress-strain curves by calculating the strain and stress through the following equations:

$$\boldsymbol{Stress}: \ \sigma = \frac{F}{A} \tag{4.2}$$

$$\boldsymbol{Strain}: \ \varepsilon = \frac{\Delta L}{L_0} \tag{4.3}$$

Where:

σ – Stress (MPa)

ε – Strain

F – Force (N)

A – Area (mm²)

ΔL – Displacement (mm)

L_0 - Initial length (mm) (distance between the mechanical folds before the test)

The calculated stress was apparent since the area was considered equal to the diameter of the filament (since the meshes are only composed of 1 layer) multiplied by the width of the sample (10 mm).

Figure 31 illustrates a representative stress–strain curve, from which a wide range of material properties can be derived. Elastic deformation refers to the reversible response of a material, whereby the induced strain is recovered upon the removal of the applied stress. Within the stress–strain curve, this behavior is characterized by the initial linear region, in which stress (σ) is directly proportional to strain (ε).

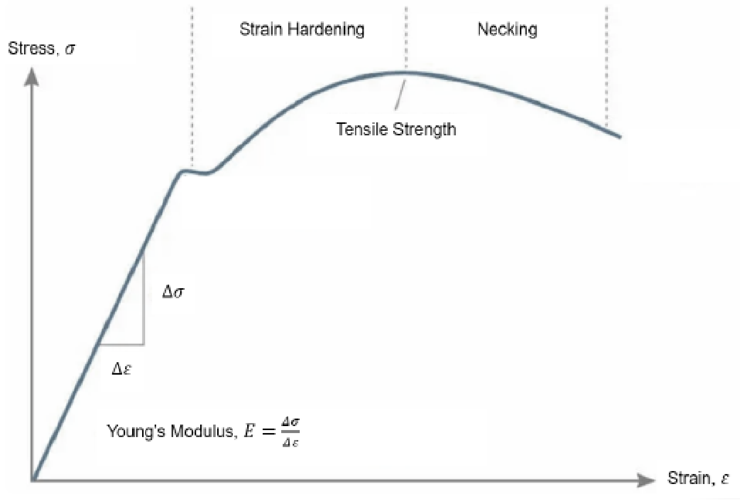

Figure 31 *Schematic of a typical Stress-Strain curve* [8].

Young's modulus (E), also referred to as the elastic modulus, is a fundamental mechanical property that reflects the stiffness of a material by quantifying its resistance to elastic deformation under load. It is defined as the ratio of the applied stress to the corresponding strain within the linear elastic region of the stress–strain curve. This mechanical property is usually expressed in MPa and is calculated by the Equation 4.4:

$$E = \frac{\sigma}{\varepsilon} \tag{4.4}$$

From a uniaxial point of view, conventional meshes tend to have greater initial stiffness and lower deformability, with earlier failure under stretching. In contrast, auxetic meshes are characterized by lower initial stiffness, followed by greater deformation capacity before rupture, allowing greater energy absorption and behaviour closer to that of native vaginal tissue. Thus, it is expected that the greater ductility and toughness (ability of a material/structure to absorb energy before failure) of auxetic meshes will favour better biocompatibility with vaginal tissue.

4.4.2 Ball Burst Test

Ball burst testing, also known as burst strength or burst pressure testing, is a widely used method to assess a material's resistance to internal pressure until rupture occurs. Performed under standardized conditions, this technique provides reliable and reproducible data on structural integrity, making it a valuable tool for product development, quality assurance and regulatory validation in diverse sectors such as packaging, manufacturing, automotive and aerospace [4].

Unlike uniaxial tensile testing, where the applied load is directed in-plane with the specimen, the ball burst test applies an orthogonal load to the central region of the sample. As a result, while tensile testing offers information on the directional properties of a material, the ball burst method provides insight into its multiaxial mechanical behavior, thus allowing a more comprehensive evaluation of tissue structural performance [4].

The materials subjected to testing included meshes with diameters of 0.24 mm, configured in the auxetic geometries mentioned before, as well as vaginal tissue with approximately 50 mm width, 50 mm length and 4 mm thickness.

Additionally, combined tests involving vaginal tissue and meshes were conducted, with the mesh positioned inferior to the vaginal tissue, corresponding to the distal part of the vaginal wall. It is worth noting that at least three trials were conducted for each test, with mesh and tissue tests solely performed using meshes of 0.24 mm. For the ball burst tests, the crosshead speed was set to 10 mm/min in compression mode and the load cell for de meshes was a 100 N load cell but for the tissue it was used the 2500 N load cell.

In ball burst tests, which simulate multidirectional loads like those that occur *in vivo*, the differences become even more evident. Conventional meshes concentrate stresses at the puncture contact point, resulting in sudden failures and relatively low absorbed energy. Auxetic meshes, on the other hand, redistribute stress more evenly, withstanding greater displacements until failure and dissipating more energy in the process. This response suggests superior performance in localized and dynamic load scenarios, such as those experienced in the vaginal environment, where tissues are subject to complex and repetitive forces. Figure 32 illustrates how the mesh and vaginal fabric system was prepared for the ball burst tests

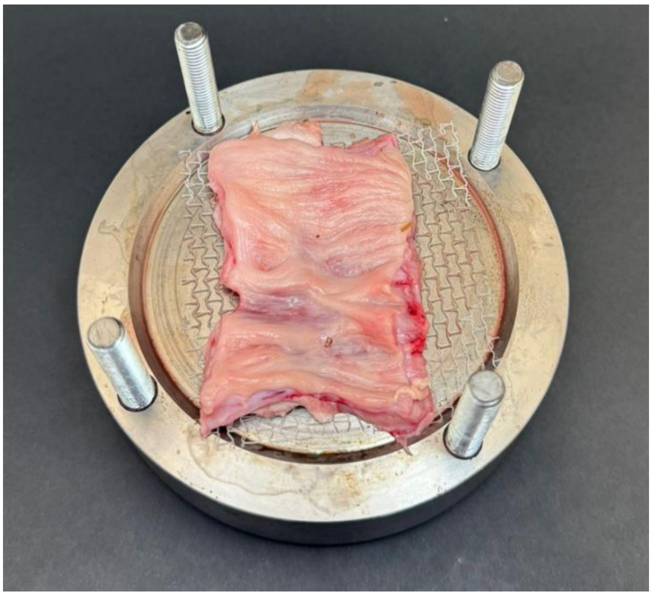

Figure 32 *Preparation of vaginal tissue with printed mesh for ball burst testing.*

Chapter 5

Mechanical tests results and Discussion

Mechanical characterization is an essential step in the evaluation of implantable devices intended for the treatment of pelvic organ prolapse, since the functional performance of these materials depends directly on their ability to withstand and respond adequately to the physiological forces to which they will be subjected in the biological environment. In addition to ensuring the structural integrity of the implant, the mechanical properties must be similar to those of native tissue, ensuring functional compatibility, minimizing the risk of complications and promoting adequate biomechanical integration.

In this study, the mechanical characterization of the auxetic meshes developed was performed using two complementary types of tests: uniaxial tests and ball burst tests.

The uniaxial tests made it possible to obtain stress-strain curves representative of the intrinsic behaviour of the materials under controlled loading in a single direction, enabling the determination of fundamental parameters such as stiffness, maximum strength and deformation at break. These tests were also essential for evaluating the effect of structural anisotropy, having been performed in two different orientations of the meshes, “auxetic direction” (cell unit of the mesh arranged vertically) and “non-auxetic direction” (cell unit of the mesh arranged horizontally), and included the characterization of native vaginal tissue as a physiological reference.

In addition, ball burst tests allowed the structural response to be evaluated under multiaxial loading conditions, which are closer to the complex forces that act *in vivo*. These tests analyzed not only the behaviour of the isolated meshes, but also the effect of reinforcing the vaginal tissue with the developed meshes, providing a more comprehensive perspective of their potential for clinical applications.

Therefore, this chapter presents the experimental results obtained from the characterization of auxetic PCL meshes and their comparison with biological tissue, Restorelle synthetic mesh (in the case of uniaxial tests), as well as with results obtained in other studies in the literature on this subject.

5.1 Results of the Uniaxial tests

5.1.1 Auxetic direction of the Meshes

In uniaxial tests, the meshes developed by MEW (re-entrant honeycomb and double arrowhead) showed distinct mechanical profiles, reflecting the decisive influence of geometry on structural response. Figure 33 shows the stress-strain curves for the uniaxial test of the meshes printed in the auxetic direction (main cell unit is in the vertical position), as well as the sow vaginal tissue used in this study.

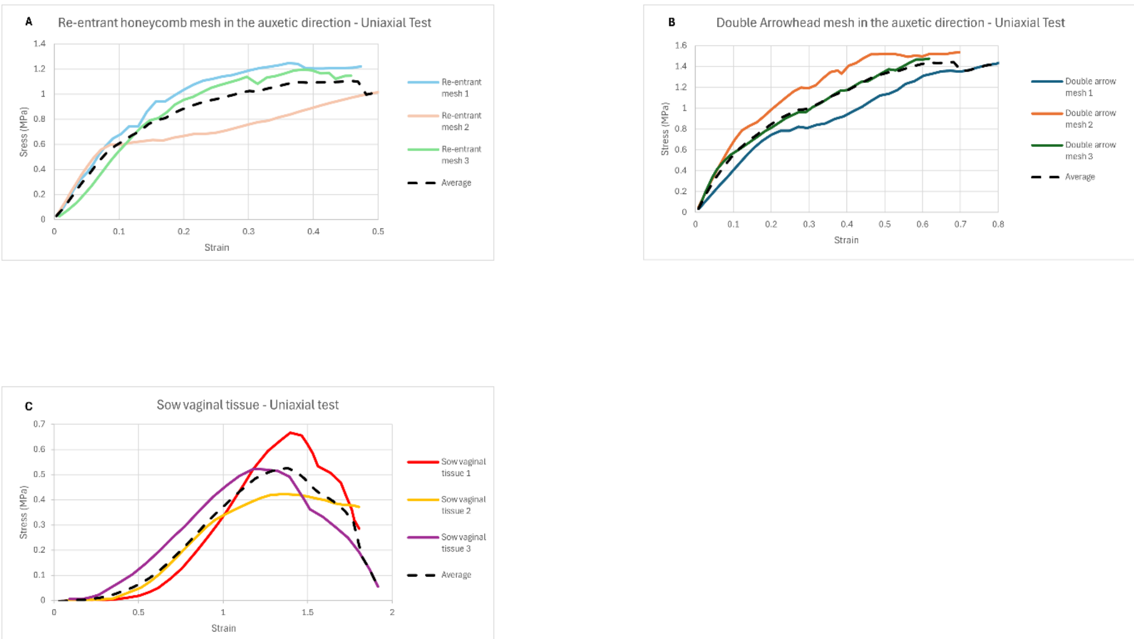

Figure 33 *Uniaxial stress-strain response of the re-entrant honeycomb mesh (A), double arrowhead mesh (B) in the auxetic directions and sow vaginal tissue (C)-is depicted along with the average response curve.*

The re-entrant honeycomb mesh exhibited an approximately linear initial response up to about 0.1 strain, followed by a non-linear hardening phase and a plateau up to approximately 0.5 strain, suggesting greater initial compliance, with its elastic limit (the point at which the material ceases to behave elastically) identified at just above 0.20 strain. The presence of a plateau-like region on the stress–strain curve suggests the occurrence of geometric strain accommodation mechanisms characteristic of re-entrant honeycomb auxetic structures. Although these mechanisms were not directly evaluated in this study, the observed behavior is consistent with that described in the literature, where the initial deformation is partially accommodated by changes in the mesh architecture before the full strength of the filaments is mobilized [93]. This combination of reduced initial stiffness and prolonged plateau suggests that the re-entrant geometry may favor energy dissipation and more harmonious integration with soft tissues [93].

The double arrowhead mesh revealed distinctive behavior, characterized by higher average strength (approximately 1.4 MPa) and superior ductility, reaching deformations of up to 0.7-0.8 before rupture, indicating greater structural robustness and greater ductility compared to the re-entrant mesh. This mesh showed a higher Young's modulus, indicating greater rigidity in the initial stages of deformation. The elastic limit is identified for strain values of 0.20, followed by progressive and continuous hardening, without the occurrence of a plateau. This behaviour gives the double arrowhead greater load capacity, although at the expense of lower initial compliance [63].

In turn, the sow vaginal tissue exhibited the non-linear behaviour characteristic of soft tissues, with an initial phase of low stiffness followed by a progressive increase in stress up to maximum values ranging between 0.5 and 0.6 MPa. This behaviour may be associated with the progressive recruitment of collagen fibers described in the literature [32]. Although it exhibited lower stress values than the meshes, the tissue displayed significantly greater strains prior to failure, highlighting its high capacity for deformation. The reduction in stress following the peak suggests the progressive development of structural damage in the tissue, in line with the behaviour generally reported for vaginal tissues.

In summary, the geometry of the mesh determined clear differences: the re-entrant proved to be more compliant and capable of dissipation (plateau), while the double arrowhead maximized strength and ductility. The fabric stood out for its much higher elongation capacity, despite its lower strength. The three repetitions per condition show a good overlap in the meshes (especially in the double arrowhead), suggesting reproducibility of manufacture and testing and greater dispersion in the tissue, consistent with biological heterogeneity (age, anatomical region and hydration).

When the interest is also to compare the behaviour of auxetic meshes in uniaxial tests with that of vaginal tissue, it becomes possible to analyze their performance in terms of functional compatibility, considering two reference zones: the “comfort zone” (deformation values up to 20%), which represents the physiological regime associated with daily activities, favouring compliance and low stiffness in this zone and the “safety zone” (deformation values between 20% and 40%), which refers to scenarios of overload and stress peaks, a zone where it is important to ensure robustness and load capacity without failure. In this regard, Figure 34 shows the uniaxial stress-strain response of the meshes being evaluated in this study (average curves), as well as the average curve of the vaginal tissue sample collected for this experimental study, the curve of the synthetic polypropylene mesh (Restorelle) and the curve referring to 4 mm thick sow vaginal tissue from another laboratory study [94].

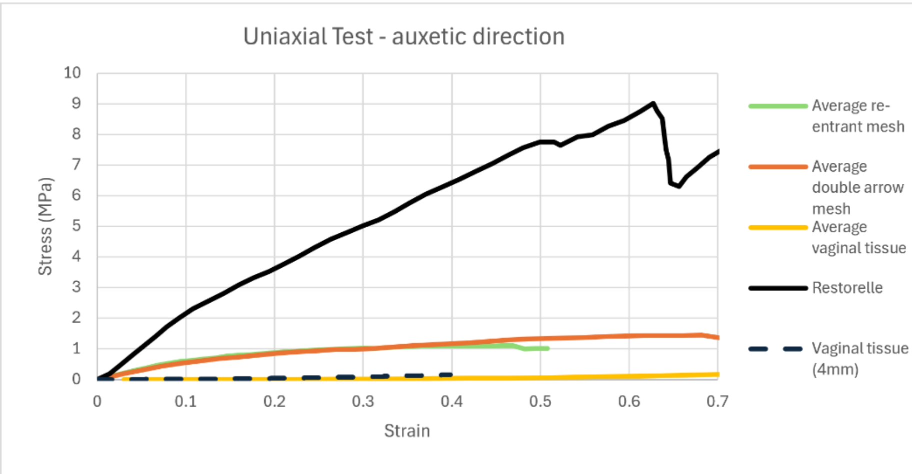

Figure 34 *The uniaxial force–strain response of the auxetic meshes in the auxetic direction compared to the obtained vaginal tissue, Restorelle synthetic mesh and sow's vaginal tissue from another study* [94].

In the comfort zone, the vaginal tissue showed the greatest compliance, exhibiting low stress values even at relatively high elongations. The reentrant mesh exhibited a stiffer mechanical response than the tissue, displaying moderate initial stiffness but a deformation profile that partially approximates the soft behaviour of the vaginal tissue. In turn, the double arrowhead mesh had a higher initial modulus, reflecting greater stiffness and, consequently, lower accommodation capacity in this physiological regime. In the safety zone, the vaginal tissue exhibited a gradual increase in stress, consistent with the nonlinear mechanical behaviour typically reported for soft biological tissues. Throughout the test, the tissue maintained lower stress levels than the auxetic meshes, reflecting its lower stiffness and higher deformability.. The re-entrant mesh exhibited characteristic accommodation behaviour, with the curve tending towards a plateau, reflecting its ability to dissipate energy and limit stress accumulation during moderate deformations. In contrast, the double arrowhead mesh demonstrated continuous hardening, with a progressive increase in stress as deformation increased, giving it greater structural robustness in this regime, although with a lower damping effect compared to the tissue. As such, the re-entrant honeycomb mesh prioritizes compatibility in everyday life and peak mitigation, while the double arrowhead mesh prioritizes structural safety in scenarios with greater mechanical demands, albeit at the expense of less comfort in the comfort zone.

A direct comparison between the two auxetic geometries revealed striking differences in mechanical behaviour. The re-entrant honeycomb mesh had a lower initial modulus and a profile characterized by an accommodation phase, evidenced by a tendency towards a plateau at intermediate deformations, which gives it greater energy dissipation capacity. In contrast, the double arrowhead mesh exhibited higher initial stiffness and progressive hardening throughout the curve, reaching higher values of maximum strength and deformation at break. Thus, while the re-entrant geometry favours greater conformability and load absorption, the double arrowhead geometry stands out for its greater structural robustness and ability to withstand more extensive deformations before failure.

Compared to Restorelle commercial mesh, both auxetic meshes are substantially less rigid, which is desirable for mechanical compatibility. In the analyzed data (Figure 34), the Restorelle mesh corresponds to the upper limit of stiffness, while the vaginal tissue represents the lower limit. The meshes developed by MEW were positioned between these two extremes, showing a compromise between compliance and structural support. The re-entrant geometry behaved more like tissue, characterized by greater accommodation capacity and a tendency to dissipate energy, while the double arrowhead geometry was closer to the structural pole, distinguished by greater load capacity and superior useful elongation before rupture.

This analysis provides the basis for a critical comparison with studies available in literature, where different configurations of auxetic meshes produced by melt electrowriting were similarly characterized, allowing us to assess the extent to which the geometries tested here replicate or diverge from previously reported trends. The re-entrant honeycomb mesh developed in this study exhibited behaviour qualitatively similar to that reported by Ferreira et al. (2025) [94] for the Evans re-entrant geometry, which is identical to the geometry printed in this work but possibly with slightly different re-entrant angles [94]. In both cases, greater rigidity than that of vaginal tissue was observed, accompanied by a regime of accommodation in intermediate deformations, associated with the auxetic mechanism of cell rotation. However, the stress values obtained in this study were higher, which can be attributed to the larger filament diameter used in printing (240 μm compared to 160 μm in the aforementioned study). The increase in the relative thickness of the filaments leads to a higher structural density of the mesh, resulting in an increase in Young's modulus and maximum strength. Thus, although the functional signature of the two geometries is congruent, the differences in absolute values confirm that filament diameter is a critical design parameter, capable of modulating the proximity of the mesh to the physiological behaviour of the tissue or, alternatively, of reinforcing its structural robustness [94].

In the study conducted by Cunha et al. (2021) [2], different geometries of PCL meshes obtained by MEW were produced and characterized, namely square (Q), triangular (T) and cross (X), in two structural configurations: one composed of 0.08 mm filaments, thinner and more flexible, and another with 0.24 mm filaments, thicker and more structural. Comparing the results obtained by Cunha et al. (2021) with the experimental results obtained in this work (Figure 34), a fundamental difference can be observed between the linear and continuous behaviour of regular meshes and the non-linear and adaptive behaviour of the developed auxetic meshes, reflecting the determining influence of geometry on the mechanical response. While the re-entrant honeycomb mesh revealed an initial elastic phase followed by a plateau at intermediate deformations, a behaviour characteristic of auxetic structures, in which rotation and reorientation of structural cells occur, promoting stress redistribution and energy dissipation [84], the regular geometries of Cunha et al. (2021) present stress-strain curves in which stress increases continuously with deformation, with no evidence of accommodation mechanisms. In turn, the behaviour of the double arrowhead mesh, with an initial stiffness greater than that of the re-entrant mesh and progressive hardening as deformation increased, without plateau formation, is similar to the.profile observed in the cross and triangular geometry meshes of Cunha et al., which also showed a continuous increase in stress with deformation.

It should be noted that, although the meshes produced by Cunha et al. (2021) with 0.08 mm filaments presented Young's modulus values similar to those of vaginal tissue in the comfort zone ($\varepsilon \leq 0.20$), this behaviour is mainly due to the reduced thickness of the filaments, and not to the existence of geometric deformation mechanisms [2]. In the present study, even using 0.24 mm filaments, the auxetic meshes demonstrated behaviour closer to that of tissue than the regular meshes of equal thickness in Cunha et al., which shows that auxetic geometry can compensate for the increase in stiffness associated with the larger filament diameter. This result confirms the predominant role of structural architecture in regulating the mechanical response of MEW implants, allowing for better functional adaptation without compromising the overall strength of the material.

In summary, the comparison between the two studies shows that the regular meshes (square, triangular, and cross) of Cunha et al. exhibit linear behaviour dependent on filament thickness, while the auxetic meshes developed in this study exhibit a non-linear and adaptive response, characterized by greater deformation capacity, energy dissipation and biomimetic behaviour. Thus, even with thicker filaments, auxetic meshes can position themselves between vaginal tissue and Restorelle in terms of stiffness, validating the potential of auxetic geometries as a design strategy for implants with better mechanical and functional compatibility.

Finally, the study conducted by Rynkevic et al. (2022) [32] aimed to characterize PCL meshes produced by MEW for application in pelvic support implants. The authors developed meshes with regular square grid geometry, varying the filament diameter between 80 µm, 160 µm and 240 µm, as well as the number of layers deposited for filaments with a diameter of 80 µm (1-3 layers) in order to evaluate the influence of these parameters on the mechanical response. The results showed that increasing the filament diameter results in a progressive increase in stiffness and maximum strength, while the thinner samples (80 µm) exhibit a response closer to that of vaginal tissue. Comparing the auxetic meshes studied in this work with square grid meshes with the same filament diameter (240 µm), the latter exhibit maximum stresses between 0.5 and 0.7 MPa up to values of 25% deformation, while, in the same deformation range, re-entrant honeycomb and double arrowhead meshes reach comparable stress values (0.8-1.0 MPa), remaining, however, well below the stiffness of Restorelle. In fact, it was observed that, for deformations up to approximately 25%, the initial stiffness of the meshes developed in this work is similar to that recorded for the 240 µm square-grid mesh reported by Rynkevic et al. (2022) [32]. This similarity is justified by the fact that, in this regime of reduced deformations, the overall behaviour is dominated by the intrinsic elastic response of the material (PCL) and the thickness of the filaments, with the contribution of the geometric mechanisms characteristic of auxetic structures still being limited. In this initial phase, deformation occurs essentially by elongation of the individual filaments, without significant rotation or opening of the cells, which results in similar effective Young's modulus values between meshes of different geometries, provided they share the same material and filament diameter.

For higher deformations, the differences between geometries become evident: auxetic meshes begin to exhibit a non-linear response, with plateau formation (in the case of re-entrant honeycomb) and increased deformability (in the case of double arrowhead), while the square-grid mesh maintains monotonic hardening. This behaviour confirms that auxetic geometry plays a decisive role in intermediate to high deformation regimes, when the mechanisms of rotation and reorientation of cellular units are fully activated. These results confirm that, for the same material and filament diameter, auxetic architecture increases useful deformability and introduces stress dissipation/redistribution mechanisms that do not exist in regular meshes, positioning the developed structures between the tissue curve and the upper limit represented by Restorelle.

On the other hand, although both studies present the same filament diameter, the pore size is different. In the present study, as mentioned above, the pore size is 3 mm, while in the study by

Rynkevic et al. (2022) the pore size is 2 mm [32]. This difference also influences the mechanical response of the meshes. In fact, as the pore size decreases, the number of columns in the mesh increases (increase in relative density), making the mesh more resistant to the applied force, resulting in higher load-displacement values.

Therefore, it was expected that meshes with a 3 mm pore size would exhibit a lower initial modulus and lower stresses for the same deformation compared to 2 mm square grids. However, the stress levels observed in the auxetic study up to 25% deformation are not substantially lower. This results from the predominance, in this range of values, of the elastic regime of the material, as well as topological differences in the load paths, i.e., due to the way the mesh is designed, some filaments are better aligned with the direction of traction, causing them to immediately begin to resist the load, increasing the initial stiffness of the curve. In addition to these two parameters, some experimental factors may also justify the differences observed, such as stress normalization (the cross-sectional area of the sample may be different; when considering a smaller area, there is an increase in the stress value) and geometric fidelity, i.e., small actual variations (slightly thicker filaments due to the manufacturing process, which causes material overlaps in certain areas, leading to an increase in thickness and resistance to deformation) can also make the mesh more resistant than expected.

In summary, increasing pore size attenuates stiffness as predicted by cellular structure models, but auxetic architecture modulates the mode of deformation, introducing energy dissipation (re-entrant honeycomb) or greater structural reserve with high extensibility (double arrowhead), effects that are not observed in regular square grids.

5.1.2 Non-Auxetic direction of the Meshes

As described in Chapter 4, the uniaxial tests were performed in two loading directions. This section presents the results obtained in the non-auxetic direction, in which the unit cells of the meshes are oriented horizontally with respect to the loading axis. The results are shown in Figure 35. Graph A presents the stress–strain curves of the re-entrant honeycomb mesh and its average response, while Graphs B and C show the responses of the double arrowhead mesh and sow vaginal tissue, respectively. Since the vaginal tissue results correspond to the same dataset discussed in the previous section, only a brief comparison will be provided here.

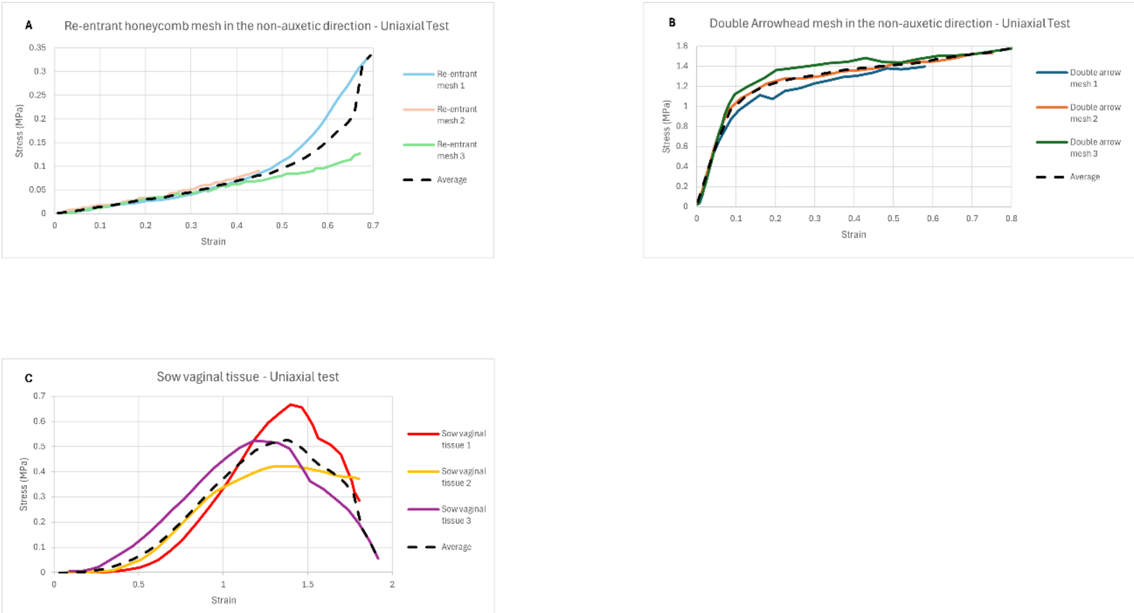

Figure 35 *Uniaxial stress-strain response of the re-entrant honeycomb mesh (A), double arrowhead mesh (B) in the non-auxetic directions and sow vaginal tissue (C)-is depicted along with the average response curve.*

The re-entrant honeycomb mesh tested in the non-auxetic direction exhibited a highly compliant mechanical response, characterized by low stress values throughout the deformation range analyzed. The average stress–strain curve showed a gradual increase in stress with increasing deformation, reaching a maximum stress of approximately 0.33 MPa. Compared with the response observed in the auxetic direction, substantially lower stress values were obtained, highlighting the anisotropic behaviour of the structure. This response suggests that the mesh is able to accommodate relatively large deformations while developing comparatively low stress levels, resulting in more deformable mechanical behaviour. Such behaviour is consistent with the influence of the geometric architecture of the re-entrant honeycomb structure on its mechanical response under tensile loading.

In contrast, the double arrowhead mesh exhibited a markedly stiffer mechanical response, characterized by higher stress values throughout the entire deformation range analyzed. The average stress–strain curve showed a steeper initial slope and reached maximum stress values substantially higher than those observed for the re-entrant honeycomb mesh. These results indicate a greater resistance to deformation when loaded in the non-auxetic direction. The clear differences between the two geometries highlight the strong influence of structural architecture on the mechanical behaviour of the meshes, with the double arrowhead configuration providing a significantly higher load-bearing capacity under uniaxial loading conditions.

When compared to sow vaginal tissue, the two geometries exhibit distinct behaviours in both relevant functional zones: the comfort zone ($\varepsilon \leq 0.20$), associated with physiological deformations typical of the pelvic floor during daily activities, and the safety zone ($0.20 < \varepsilon \leq 0.40$), related to occasional load peaks. The re-entrant honeycomb mesh exhibits very low average stress throughout the test, remaining below 0.05 MPa in the comfort zone and below 0.10 MPa in the safety zone. These values are close to those recorded for vaginal tissue, which exhibits stresses below 0.1 MPa at deformations up to 0.20, demonstrating a high capacity for mechanical accommodation. This similarity suggests that the re-entrant may offer more biomimetic behaviour, minimizing the risk of mechanical incompatibility with adjacent tissues. The double arrowhead mesh, in contrast, exhibits substantially higher stress values than the tissue in both regimes. In the comfort zone, the average stress reaches about 1.2 MPa, and in the safety zone it approaches 1.4 MPa, values that greatly exceed those observed in vaginal tissue. This response indicates a stiffer and less deformable mesh, which may translate into greater structural support capacity, but also into lower mechanical compatibility with native tissue. Nevertheless, its performance may be advantageous in clinical situations where additional support to prolapsed tissue is required.

In summary, the re-entrant honeycomb mesh stands out for its high flexibility and similarity to the behaviour of vaginal tissue, which makes it potentially more suitable for applications where mechanical biocompatibility is a priority. On the other hand, the double arrowhead mesh exhibits a robust structural response and greater support capacity, characteristics that may be desirable in clinical contexts that require more pronounced mechanical reinforcement.

Figure 36 represents the uniaxial stress-strain response of the meshes being evaluated in this study (average curves) in the “non-auxetic direction”, as well as the average curve of the vaginal tissue sample collected for this experimental study, the curve of the synthetic polypropylene mesh (Restorelle) and the curve referring to 4 mm thick sow vaginal tissue from another laboratory study [94]. As in the previous section, this section also discusses the results obtained in this mesh direction based on the articles in the literature analyzed above.

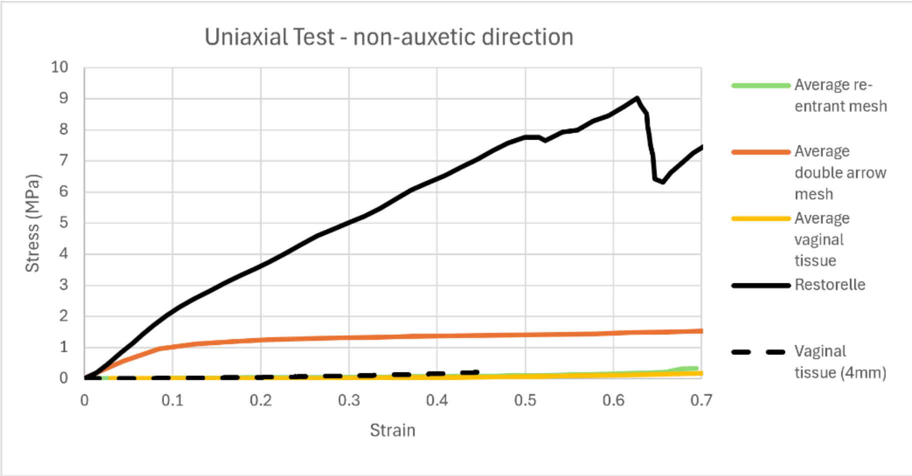

Figure 36 *The uniaxial stress–strain response of the auxetic meshes in the non-auxetic direction compared to the obtained vaginal tissue, Restorelle synthetic mesh and sow's vaginal tissue from another study* [94].

The analysis of the re-entrant honeycomb mesh in the “non-auxetic direction” reveals behaviour that differs from that reported by Ferreira et al. (2025) [94] for the Evans re-entrant mesh. In this orientation, the stress-strain curve is characterized by very low initial stresses, absence of plateau and a globally more passive and flexible mechanical response, in contrast to the curve presented in the aforementioned study, which shows a progressive increase in load and a plateau regime associated with the gradual activation of auxetic mechanisms. This discrepancy demonstrates that, in the horizontal orientation, the re-entrant geometry loses much of its lateral expansion capacity, with deformation dominated by bending and limited rotation of the filaments, with reduced structural mobilization. In fact, given the results obtained in the article in question, the mechanical behaviour of the re-entrant honeycomb mesh when its cellular unit is arranged horizontally resembles that described for square-grid and three-star honeycomb meshes. That is, as reported for the meshes mentioned, the mesh studied in this work, in this direction, exhibits hyperelastic behaviour, withstanding small loads, distributing mechanical stress more uniformly, maintaining compliance and adaptability, and positioning the geometry in this orientation in a manner that is more biomechanically compatible with the tissue; this may help to reduce implant-related complications, such as inflammation and mesh contraction [94].

The analysis of the mechanical behaviour of the meshes developed in this work in the “non-auxetic direction” shows significant differences compared to the regular geometries studied by Cunha et al. (2021) [2]. The re-entrant honeycomb mesh showed a response characterized by low initial stiffness and gradual stress growth throughout deformation, remaining below the curves obtained for the square, triangular and cross-shaped meshes reported by Cunha. This behaviour, distinct from that observed in the “auxetic direction”, results from the directional nature of the re-entrant geometry, in which, in this orientation, the structural mechanisms may be associated with cell rotation and filament bending overlap with direct stretching, leading to lower developed stresses. Furthermore, the use of a filament diameter of 240 μm, identical to that of some configurations tested by Cunha, suggests that the differences observed are mainly due to the geometric behaviour of the structure and the orientation of the loading, and not only to the thickness of the filament.

In contrast, the double arrowhead mesh shows a sharp rise at the beginning, followed by almost linear growth up to deformation values of 0.8, resulting in a structural profile more similar to the behaviour of the regular 240 μm meshes studied in the article up to deformation values of 0.25 (range of values studied by Cunha et al. (2021)). This performance shows that the double arrowhead geometry maintains effective load paths even in this orientation, being less sensitive to the loading direction than the re-entrant and showing more predictable and resistant structural behaviour.

A comparison of the results obtained for the meshes developed in this study in the “non-auxetic direction” with those presented by Rynkevic et al. (2022) [32] reveals significant differences in overall mechanical behaviour, directly related to structural geometry, unit cell orientation relative to loading and morphological manufacturing parameters. In the aforementioned study, PCL meshes with a filament diameter between 80 μm and 240 μm and a pore size of approximately 2 mm were produced, whose mechanical response presented maximum stress values in the order of 0.5–1.0 MPa and deformations up to about 0.25, with almost linear behaviour across the entire range analyzed. When comparing the meshes from the aforementioned study with 240 μm of fiber diameter with the auxetic meshes from this study, the re-entrant honeycomb mesh revealed a significantly more compliant profile in this orientation, with stresses below 0.05 MPa in the same deformation range. This deviation was expected, since the larger pore size used (3 mm) reduces the relative density and, consequently, the stiffness of the structure. Furthermore, the “non-auxetic orientation” compromises the activation of the structural mechanisms characteristic of this geometry, resulting in behaviour dominated by filament bending and rotation phenomena, which are less efficient in load transfer and contribute to a reduction in overall strength.

On the other hand, the double arrowhead mesh showed different behaviour, with a steeper initial rise and an almost linear structural response, reaching stresses of around 1.2 MPa at 25% deformation and maximum values close to 1.4 MPa. These results exceed those obtained for the 240 μm meshes of Rynkevic et al. (2022), despite the larger pore size, suggesting that the geometric configuration of this mesh allows for more direct and efficient load trajectories even in this orientation, compensating for the reduction in stiffness associated with lower structural density. This behaviour can be associated with a lower directional sensitivity of the double arrowhead mesh, which maintains robust mechanical properties in both loading directions.

5.1.3 Comparison of both directions of the meshes

To conclude the analysis of the uniaxial mechanical tests, Figure 37 presents the average stress–strain curves obtained for both loading directions of each mesh. This comparison enables the evaluation of the directional dependence of the mechanical response and provides a better understanding of the anisotropic characteristics associated with the auxetic geometries

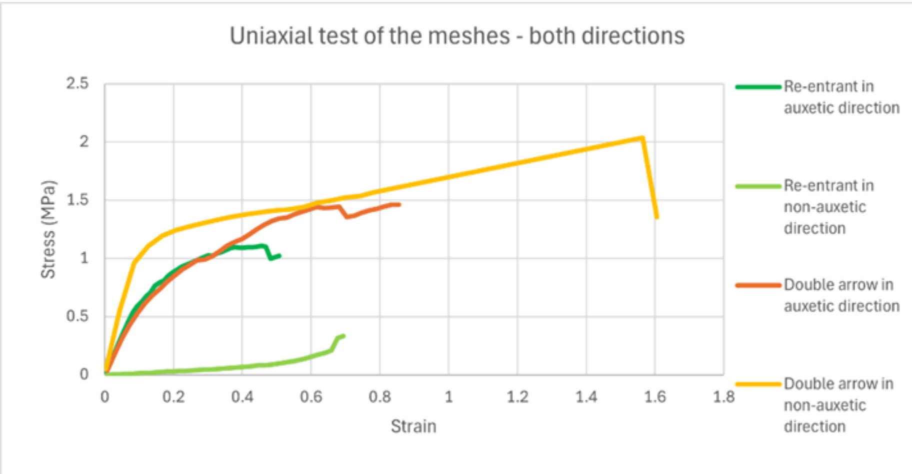

Figure 37 *Comparison of the uniaxial stress-strain response of the two auxetic mesh geometries in both directions.*

Comparative analysis of the stress–strain curves obtained in the two main loading directions reveals the significant impact of cell orientation on the overall mechanical performance of the developed auxetic meshes. This assessment is essential for understanding the degree of structural anisotropy and the extent of auxetic behaviour in both directions.

The re-entrant honeycomb mesh exhibits markedly directional behaviour, with substantial differences between the responses obtained in the auxetic and non-auxetic directions. In the "auxetic direction" (cell unit oriented vertically relative to the load), the curve is characterized by a progressive increase in stress up to about 1.0-1.2 MPa, followed by a plateau regime that may be associated with the characteristic deformation mechanisms of the re-entrant geometry reported in the literature. This behaviour translates into an increased capacity for deformation accommodation and energy dissipation, maintaining moderate stress levels even at higher deformations.

In contrast, in the “non-auxetic direction” (cell unit arranged horizontally), the mechanical response of the reentrant is substantially more flexible and less resistant, with average stresses below 0.5 MPa throughout the entire test. The curve shows a slow and continuous increase in stress, and this difference may demonstrate that the auxetic behaviour of the reentrant depends heavily on the orientation of the cells and manifests itself mainly when the mesh is subjected to stress along its preferred structural direction.

Thus, the re-entrant honeycomb can be classified as strongly anisotropic, exhibiting pronounced auxetic behaviour only in the vertical direction.

The double arrowhead mesh demonstrates more balanced behaviour between the two directions, although significant differences are also observed. In the “auxetic direction”, the curve has a non-linear profile typical of structural materials with adaptive geometry, reaching maximum stresses of around 1.4 MPa and revealing a combination of initial stiffness and significant deformation capacity. The progressive increase in stress suggests that the auxetic mechanism is active, although less pronounced than in the case of the re-entrant.

In the “non-auxetic direction”, the double arrowhead mesh exhibits an even more robust response, with maximum stress values close to 2.0 MPa and a substantially higher useful deformation, values around 1.5. This response indicates that, even outside its preferred orientation, the mesh maintains a resistant structure with high load-bearing and deformation capacity. Although the auxetic signature is less evident in this direction, overall performance remains high, suggesting that the double arrowhead geometry is less sensitive to cell orientation and maintains functional characteristics in both directions.

In summary, the double arrowhead exhibits quasi-isotropic behaviour, combining stiffness and high deformability in both directions tested, although the degree of auxeticity is slightly higher in the vertical orientation.

The overall comparison shows that both meshes exhibit functional anisotropy, albeit to varying degrees. The re-entrant honeycomb reveals a strong directional dependence, while the double arrowhead mesh's high mechanical performance in the “non-auxetic direction” can be explained by its intrinsic geometric configuration, which includes structural elements oriented more closely to the direction of the load. This orientation favours early mobilization of the filaments under tension, even when the cell unit is arranged horizontally, ensuring efficient stress distribution and a robust structural response. In addition, the presence of multiple load paths contributes to reducing directional sensitivity and mitigating performance loss outside the preferred direction. Consequently, the double arrowhead exhibits lower functional anisotropy and more stable load capacity in both orientations, which is an important advantage for clinical applications that require multidirectional performance.

5.2 Results of the Ball Burst Test

5.2.1 Mesh

The mechanical response of auxetic meshes during ball-burst tests is described in the Load (N)/Punch (mm) graphs in Figure 38. Graph A corresponds to the re-entrant honeycomb mesh, while Graph B corresponds to the double arrowhead mesh. For each mesh, the three individual test curves and the corresponding average curve are presented.

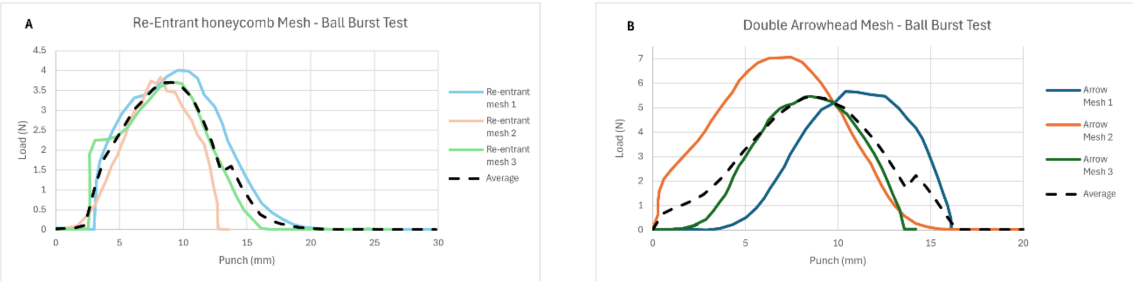

Figure 38 *Mechanical behaviour of the Re-entrant honeycomb mesh (A) and Double arrowhead mesh (B) during a ball burst test-is depicted along with the average.*

The re-entrant honeycomb mesh exhibited behaviour characterized by an average maximum load of approximately 3.7 N and an associated deformation of almost 10 mm of punch displacement, demonstrating a relatively flexible and gradual response to loading. The curve profile shows a progressive increase in load up to the peak, followed by a relatively abrupt decline, indicative of structural failure after maximum deformation. The presence of a longer plateau before the decline reflects the ability of the re-entrant geometry to dissipate energy through geometric deformation, which is consistent with its auxetic nature and more compliant behaviour.

On the other hand, the double arrowhead mesh shows superior maximum resistance, reaching average values around 5-6 N, associated with a deformation at break close to 8 mm. The resulting curve shows a steeper load increase, revealing superior structural rigidity and greater load-bearing capacity, characteristics associated with its denser and more robust architecture. This more rigid mechanical response suggests a more effective adaptation to conditions where high puncture resistance and tissue containment are required.

In order to facilitate comparison of the meshes under study in terms of their mechanical behaviour in this test, Figure 39 shows the average curves for each mesh.

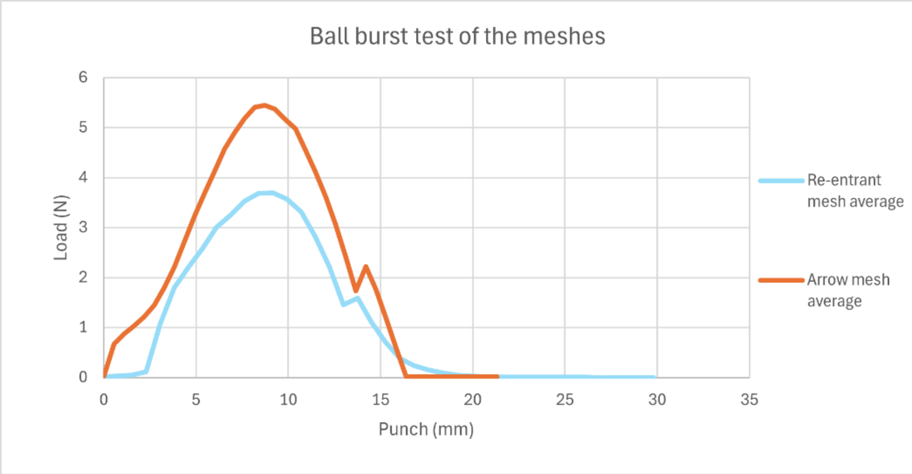

Figure 39 *Average load-punch curves of the auxetic meshes.*

The comparative analysis of the average load versus displacement curves obtained in the ball burst tests (Figure 39) shows significant differences in the structural behaviour of the two auxetic meshes developed – re-entrant honeycomb and double arrowhead – reflecting the influence of geometry on their mechanical response under multiaxial loading.

The re-entrant honeycomb mesh exhibited more progressive and ductile behaviour, reflected in a more gradual increase in load up to the peak and a smoother descent after this point. Despite withstanding a lower maximum load, the re-entrant mesh demonstrated a similar displacement capacity at the moment of rupture compared to the double arrowhead mesh, with values close to 8-10 mm. This result indicates that, although less resistant, the re-entrant mesh can accommodate significant deformations before failure, suggesting a more compliant mechanical response.

The double arrowhead mesh revealed a substantially higher maximum load capacity, reaching values close to 5-6 N, in contrast to the 3.7 N recorded for the re-entrant honeycomb mesh. This difference highlights the greater stiffness and load-bearing capacity of the double arrowhead geometry, which may be attributed to its geometric configuration. The shape of the curve shows a steep initial gradient, indicating a rapid increase in stiffness with loading, followed by a pronounced peak and a rapid post-peak decrease in load, indicating a less progressive failure process than that observed for the re-entrant honeycomb mesh.

Thus, direct comparison reveals two complementary mechanical profiles. The double arrowhead mesh stands out for its high puncture resistance and greater load-bearing capacity, indicating enhanced mechanical support. In contrast, the re-entrant honeycomb mesh exhibits greater flexibility and deformation capacity, which may favour mechanical compatibility with soft tissues. The similarity in displacement at failure suggests that both geometries maintain a favourable balance between strength and deformability, although through distinct structural strategies.

5.2.2 Vaginal tissue

The results of the ball burst test on the sow's vaginal tissue (Figure 40) were obtained from three tests, with the tissue having nearly the same dimensions in both cases, measuring 50x50 mm and 4 mm in thickness. It is important to mention that special attention was given to select a uniform location of the sample for testing.

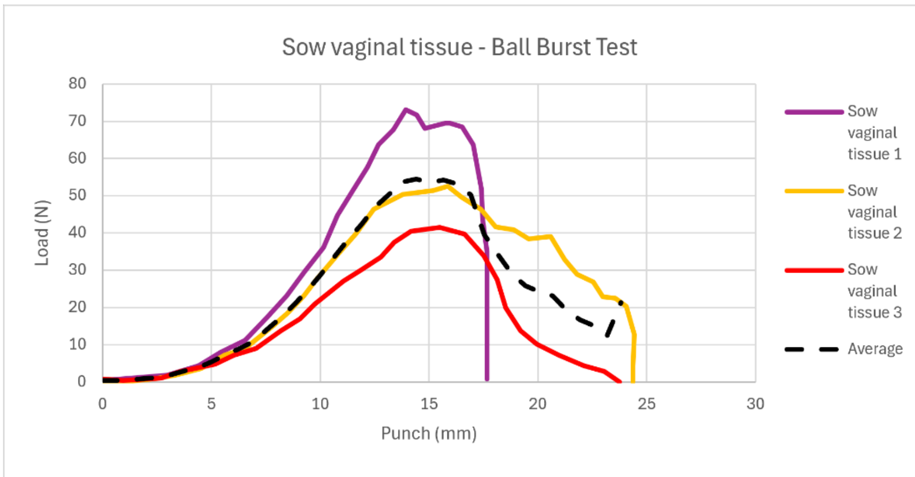

Figure 40 *Mechanical behaviour of the vaginal tissue during a ball burst test-is depicted along with the average.*

Analysis of the load-displacement curves obtained from ball burst tests carried out on isolated porcine vaginal tissue (Figure 40) revealed non-linear mechanical behaviour characteristic of soft biological tissues. In all samples, an initial phase of low stiffness was observed, followed by a progressive increase in strength as the displacement imposed by the puncture increased.

The average curve showed a maximum load of around 55 N for a displacement of approximately 15 mm. Beyond this point, a gradual reduction in the load-bearing capacity was observed, indicating the occurrence of structural damage and a consequent progressive loss of the tissue's load-bearing capacity. The fact that the maximum load occurred only at relatively high displacements demonstrates the high deformability of the vaginal tissue prior to failure, an important characteristic for accommodating the physiological deformations associated with the supportive function of the pelvic organs.

Despite this overall trend, there was considerable variation amongst the three samples tested. The maximum loads ranged approximately from 40 N to 70 N, and significant differences were also observed in the shape of the curves and in their behaviour after the peak load. Whilst sample 1 exhibited the highest strength and an abrupt loss of load-bearing capacity after failure, samples 2 and 3 showed lower maximum values and a more gradual reduction in the load they could withstand.

In fact, the variability observed between the curves obtained for vaginal tissue cannot be attributed solely to the age of the animals, as this is not a parameter that differentiates between samples. A more likely explanation relates to the intrinsic heterogeneity of vaginal tissue, which exhibits local variations in thickness, structural composition and the orientation of its constituent fibres. Furthermore, small differences in the anatomical location of the sample collection may result in significant alterations to the mechanical properties, as the vaginal wall does not have a uniform structure throughout the vaginal canal. Furthermore, the anisotropic behaviour of this tissue, combined with any differences introduced during sample preparation and fixation, may also have contributed to the dispersion observed in the experimental results. Despite the experimental variability observed, all samples exhibited a similar mechanical response, characterized by high deformability prior to failure and the ability to withstand moderate loads under localized loading.

As was done in the discussion of the uniaxial test results, it is important to compare the results obtained in the ball burst tests with the studies conducted in this field that are present in the literature. Figure 41 shows the average curve of the porcine vaginal tissue obtained in this study and the average curve of the vaginal tissue obtained in the study conducted in Jorge's dissertation [4].

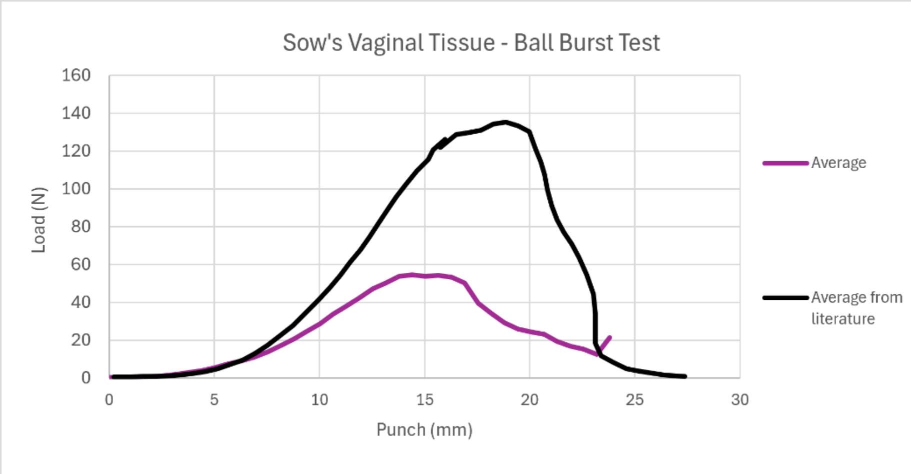

***Figure 41** Comparison of ball burst test results on tissue with Jorge's study* [4].

When comparing the average curve obtained in the present study with the average curve reported in Jorge's thesis for porcine vaginal tissue, there are significant differences in the mechanical response observed during the ball burst tests. Whilst the tissue analysed by Jorge exhibited a maximum load of around 140 N, reached at a displacement of approximately 20 mm, the average curve obtained in this study revealed a maximum load of around 60 N, at a displacement of approximately 15 mm. These results indicate that the tissue tested in this study exhibited substantially lower strength than that reported in the literature, although it retained a relatively high capacity for deformation prior to failure. Apart from the difference in maximum load, it can be seen that both curves have a similar overall shape, characterised by an initial phase of gradual increase in load followed by a decrease in load-bearing capacity once structural damage has occurred. However, the curve obtained by Jorge shows a more pronounced increase in load and a significantly higher peak, suggesting a greater capacity of the tissue to withstand localized stress prior to rupture.

Although the specimens analyzed in the present study and those reported by Jorge were harvested from the same anatomical region and presented similar dimensions, the tissues originated from different animal cohorts and were collected at different time points. Therefore, biological variability between animals may have contributed substantially to the differences observed in the mechanical response. Variations in tissue composition, collagen content, physiological condition and other animal-specific factors may influence the load-bearing capacity of vaginal tissue, even when similar experimental protocols are employed. In this regard, a limitation of this study is the relatively small number of specimens tested for each configuration (n = 3). Future work should include a larger sample size to reduce the influence of biological variability and provide a more robust assessment of the mechanical performance of the reinforced tissue–mesh systems.

Soares et al. (2022) [95] characterized the mechanical behaviour of the vaginal wall of sows subjected to ball burst tests, both without reinforcement and reinforced with cog threads, in order to assess its resistance and deformation capacity in the context of pelvic organ prolapse treatment. To this end, the authors performed ball burst tests on samples of porcine vaginal tissue, measuring the maximum force supported, the displacement at the point of rupture and the stiffness in different regions of the curve. The curves obtained allowed differences between native and reinforced tissue to be identified, showing that the addition of cog threads increases resistance and stiffness without significantly compromising deformation capacity.

Soares et al. (2022) reported a maximum load of 108.9 ± 9.76 N and a deformation at maximum load of 17.60 ± 0.72 mm for unreinforced vaginal tissue ($p < 0.05$) [95]. Comparing these results with those obtained in the present study, the vaginal tissue tested exhibits a load-bearing capacity substantially lower than that reported by Soares et al. for native vaginal tissue. However, the displacement corresponding to the maximum load was relatively close to the deformation at maximum load reported by the authors, suggesting a similar capacity of the tissue to accommodate large deformations prior to failure.

The differences observed between the results may be related to inherent variations in the biological specimens used, including variations in the anatomical location of the sample and in the structural characteristics of the vaginal tissue. Furthermore, factors associated with the experimental conditions and the configuration of the ball burst test may influence the distribution of stresses and, consequently, the maximum load values obtained. These aspects should be considered when comparing results from independent studies.

In summary, although the vaginal tissue tested in this study exhibited substantially lower maximum load values than those reported by Jorge and Soares et al., the overall load–displacement response followed the same qualitative pattern, characterized by progressive load increase, peak load attainment and subsequent structural failure. However, the considerable quantitative differences observed highlight the influence of biological variability and reinforce the need for caution when comparing results obtained from different animal cohorts.

5.2.3 Vaginal tissue reinforced with mesh

Analysis of the results obtained in ball burst tests for vaginal tissue reinforced with re-entrant honeycomb (A) and double arrowhead (B) meshes reveals striking differences in the mechanical behaviour of the two configurations tested, as shown in Figure 42.

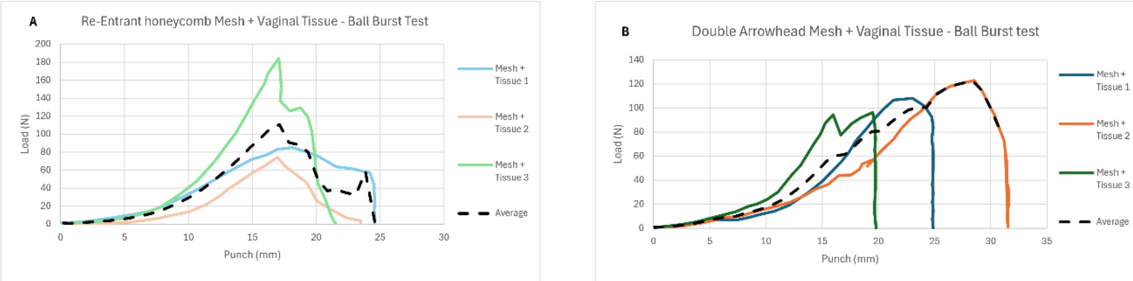

Figure 42 *Mechanical behaviour of vaginal tissue reinforced with Re-entrant honeycomb mesh (A) and Double arrowhead mesh (B) during a ball burst test-is depicted along with the average.*

The load-displacement curves obtained from the ball burst tests carried out on vaginal tissue reinforced with the re-entrant honeycomb and double arrowhead auxetic geometries reveal significant differences in the mechanical response of the tissue-mesh system, demonstrating the influence of the structure's geometry on the overall behaviour of the reinforcement.

In the case of the re-entrant honeycomb configuration, the average curve showed a progressive increase in load until reaching a maximum value of around 110 N for a puncture displacement of approximately 15–20 mm. However, considerable variation was observed between the tests carried out, particularly in the region corresponding to the maximum load. Whilst two of the specimens exhibited maximum values ranging from approximately 75 N to 90 N, the third specimen reached a significantly higher maximum load, close to 180 N. This variability suggests a greater sensitivity of the mechanical response to specimen-specific factors, although the exact origin of this variability cannot be determined from the present results.

In turn, the double arrowhead configuration exhibited significantly more uniform behaviour across the three tests carried out. The individual curves followed similar trajectories throughout the test, reaching maximum loads of between 95 N and 120 N for displacements to failure ranging from approximately 20 mm to 30 mm. The low variation observed between the samples indicates greater consistency in the mechanical response and suggests a more consistent mechanical response of the tissue–mesh system.

A comparison of the average load-displacement curves for the two geometries reveals two fundamental differences. Firstly, the double arrowhead structure exhibited a maximum load slightly higher than that obtained for the re-entrant honeycomb geometry, indicating a similar or marginally higher load-bearing capacity under localized loading. However, the most significant difference relates to deformation capacity. Whilst the re-entrant honeycomb configuration reached its maximum load at a displacement of around 18 mm, the double arrowhead configuration maintained its load-bearing capacity up to displacements of around 30 mm, demonstrating a greater ability to accommodate deformation before failure occurs.

These differences may be related to the distinct deformation mechanisms characteristic of each auxetic geometry. The re-entrant honeycomb structure appears to promote a stiffer response, leading to a more rapid mobilization of the structure's strength and greater sensitivity to local variations in the fabric-mesh system. In contrast, the double arrowhead geometry appears to favour a more gradual redistribution of stresses throughout the structure, enabling the load-bearing capacity to be maintained at higher levels of deformation and contributing to a more stable and reproducible mechanical response.

To understand whether the meshes effectively reinforced the sow's vaginal tissue, Figure 43 shows the average curve obtained from the sow's vaginal tissue, as well as the two average curves of the tissue reinforced with each of the meshes under study.

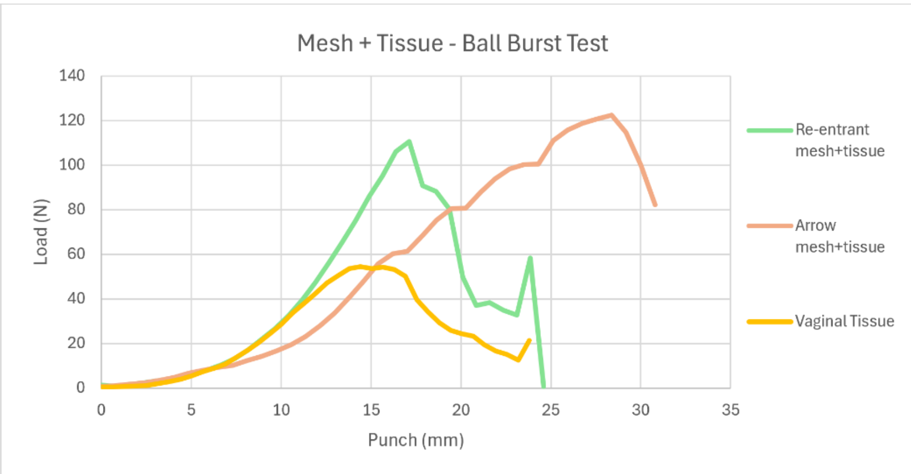

Figure 43 *Average load-punch curves of auxetic meshes and vaginal tissue.*

A comparison of the average curves obtained for the isolated vaginal tissue and for the reinforced tissue-mesh systems clearly highlights the effect of auxetic structures on the mechanical behaviour of the assembly when subjected to the ball burst test. Both geometries resulted in an increase in load-bearing capacity compared with the native tissue, demonstrating their reinforcing capacity under localised loading.

The isolated vaginal tissue exhibited an average maximum load of approximately 55 N for a displacement of approximately 15 mm, followed by a progressive reduction in load-bearing capacity. When reinforced with the re-entrant honeycomb geometry, a substantial increase in the maximum load was observed, reaching values close to 110 N, corresponding to approximately double the strength exhibited by the unreinforced tissue. This result demonstrates that the presence of the honeycomb structure contributed significantly to the redistribution of the stresses applied by the punch, enabling the system to withstand higher loads before failure occurred.

In turn, the system reinforced with the double arrowhead geometry exhibited the best overall performance, achieving maximum loads of around 120 N for displacements exceeding 25 mm. In addition to the increase in mechanical strength, this configuration demonstrated a significantly higher deformation capacity than that observed in both the fabric alone and the re-entrant honeycomb configuration. This behaviour suggests that the double arrowhead geometry enabled a more efficient load transfer between the mesh and the fabric, whilst maintaining the system's ability to accommodate high deformations without premature loss of structural integrity.

A direct comparison between the two geometries shows that both were effective in reinforcing the vaginal tissue, as they significantly increased the maximum load borne by the system. However, whilst the re-entrant honeycomb geometry essentially provided an increase in mechanical strength, the double arrowhead geometry combined this reinforcement with a substantially greater capacity for deformation. This difference is particularly relevant in the context of treating pelvic organ prolapse, where the aim is not only to increase the strength of the tissue but also to preserve its capacity for physiological deformation and to avoid excessive stress concentrations that could compromise the integration of the implant.

Overall, the results suggest that both auxetic structures have potential for use in vaginal reinforcement. However, the double arrowhead geometry showed the most promising behaviour, not only because of its high load-bearing capacity, but above all because it provides a more favourable balance between mechanical support and deformability. These characteristics are desirable in implants intended for the treatment of pelvic organ prolapse, as they allow the affected tissue to be reinforced without unduly restricting its mobility and ability to adapt to physiological stresses.

Regarding the work carried out in Jorge's dissertation [4], the ball burst tests that included mesh and tissue involved sow vaginal tissue reinforced with two mesh geometries with a filament diameter of 240 μm, square mesh and cross mesh. The differences between the curves obtained in this study and those obtained in the aforementioned study are shown in Figure 44.

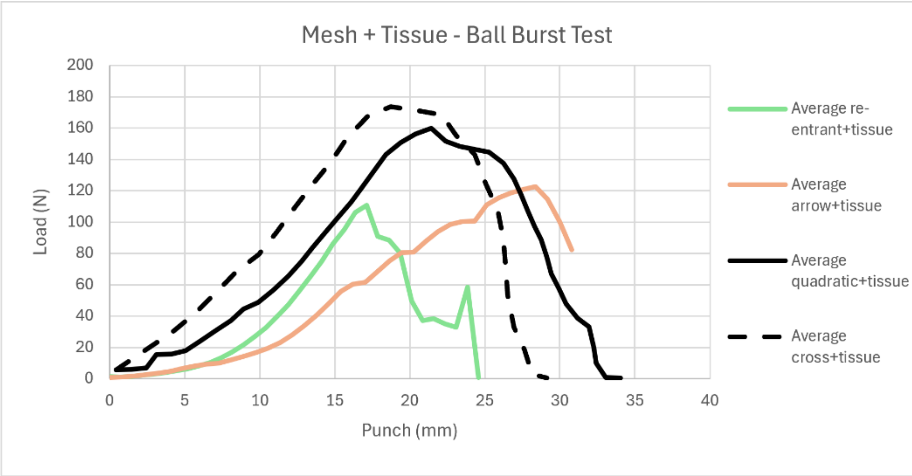

***Figure 44** Comparison of ball burst test results on tissue with meshes with Jorge's study* [4].

In general, all the configurations analyzed contributed to the reinforcement of the vaginal tissue, increasing its load-bearing capacity compared with unreinforced tissue. However, marked differences were observed in the way each geometry balanced mechanical strength and deformability.

Among the conventional meshes, the cross geometry exhibited the highest maximum load, reaching approximately 180 N for a displacement of around 20 mm. Similarly, the quadratic geometry achieved a maximum load of around 160 N for a displacement of approximately 22 mm. These results demonstrate high load-bearing capacity, a characteristic normally associated with conventional structures designed to maximize stiffness and load-bearing capacity.

Regarding auxetic geometries, the re-entrant honeycomb structure exhibited a maximum load of around 110 N for a displacement of approximately 15–20 mm, showing lower values than those observed for both conventional honeycomb structures. In turn, the double arrowhead geometry reached a maximum load of around 120 N, a value also lower than that recorded for conventional geometries. However, this structure retained its load-bearing capacity up to significantly greater displacements, close to 30 mm, revealing a substantially higher deformation capacity.

A comparison of the results suggests that conventional geometries favour the load-bearing capacity of the reinforced system, leading to higher maximum loads. In contrast, auxetic geometries, particularly the double arrowhead, exhibit distinct mechanical behaviour, characterized by a greater ability to accommodate deformations prior to failure. This behaviour is associated with the deformation mechanisms inherent in auxetic structures, which promote a more gradual redistribution of stresses across the mesh during loading.

It is important to note that the superiority of conventional geometries in terms of maximum load does not necessarily imply better performance for vaginal reinforcement applications. In the context of treating pelvic organ prolapse, the effectiveness of an implant does not depend solely on its mechanical strength, but also on its ability to accommodate the physiological deformations of the surrounding tissues. Excessively rigid structures may lead to mechanical incompatibilities and localized stress concentrations, whilst more deformable structures may promote a more homogeneous distribution of loads.

In this context, the double arrowhead geometry proved particularly interesting, as it combined considerable load-bearing capacity with the highest deformability of all the configurations analyzed. Although conventional meshes exhibited higher maximum load values, the double arrowhead structure's ability to withstand large deformations without an abrupt loss of load-bearing capacity suggests behaviour that is potentially more compatible with the biomechanical demands of pelvic floor tissues. Thus, the results obtained indicate that auxetic geometries should not be evaluated solely on the basis of the maximum load achieved, but also on their ability to provide an appropriate balance between mechanical support and deformability – characteristics that are relevant for applications in the treatment of pelvic organ prolapse.

As expected, vaginal reinforcement was also reported by Soares et al. (2022) [95], since the vaginal tissue reinforced with threads could withstand 68 N more than normal tissue, just as the auxetic geometry meshes reinforced the fabric.

Chapter 6

Conclusions and Future Works

This study contributed to the investigation of the mechanical behaviour of biodegradable meshes with auxetic geometries, evaluated through uniaxial and ball burst tests, both alone and in combination with porcine vaginal tissue. The main objective was to assess the potential of these structures for use in the treatment of pelvic organ prolapse, an area in which it is essential to ensure an appropriate balance between mechanical support and compatibility with biological tissues.

The use of non-biodegradable synthetic meshes in the treatment of pelvic organ prolapse has been replaced by biodegradable meshes, which aim to provide temporary mechanical support and promote tissue regeneration, reducing the risk of complications. Within this new generation, there are meshes with conventional geometry, which are more rigid and resistant, and auxetic meshes, which exhibit a negative Poisson's ratio, allowing greater conformability, redistribution of stress and adaptation to the movement of vaginal tissue.

The uniaxial tests revealed markedly anisotropic behaviour for both auxetic geometries, with higher values of stiffness and maximum stress observed in the 'auxetic loading direction' and a greater capacity for deformation in the 'non-auxetic direction'. These results are consistent with the deformation mechanisms characteristic of auxetic structures and confirm the influence of geometry on the mechanical response of the meshes. Among the geometries studied, the double arrowhead structure exhibited the highest stiffness and tensile strength values, whilst the re-entrant honeycomb geometry revealed a greater capacity for deformation and a more gradual behaviour up to failure. Furthermore, both auxetic meshes exhibited lower stress levels than the *Restorelle®* synthetic mesh, suggesting a mechanical response that is potentially more compatible with the surrounding biological tissues.

Ball burst tests carried out on the isolated meshes demonstrated distinct mechanical responses between the two auxetic geometries, highlighting the influence of structural architecture on behaviour under localized loading. When combined with porcine vaginal tissue, both meshes significantly increased the tissue's load-bearing capacity compared with its native state, demonstrating their ability to act as reinforcing structures. The re-entrant honeycomb configuration enabled the maximum load borne by the tissue to be approximately doubled, whilst the double arrowhead geometry achieved slightly higher load values and, more importantly, exhibited a substantially greater deformation capacity before failure occurred. In these tests, a comparison with conventional geometries described in the literature showed that the cross and quadratic mesh achieved maximum loads higher than those observed for auxetic structures. However, the double arrowhead geometry exhibited a significantly higher deformation capacity, highlighting a distinct mechanical strategy based on deformation accommodation rather than stiffness maximization. This characteristic may constitute an advantage for applications in the treatment of pelvic organ prolapse, since the implant must not only provide adequate mechanical support but also accommodate the physiological deformations of the surrounding tissues.

Overall, the results obtained indicate that both auxetic geometries have potential for use as reinforcements in the treatment of pelvic organ prolapse. However, the double arrowhead geometry stood out as the most promising configuration, combining considerable strength with the greatest deformability and the most consistent mechanical response amongst the auxetic structures studied. These characteristics suggest a favourable balance between mechanical support and conformability, which may contribute to better biomechanical compatibility with vaginal tissue and, potentially, to a reduction in complications associated with the use of excessively rigid implants.

As future prospects, it will be important to further characterize the mechanical properties of the structures developed by experimentally quantifying Poisson's ratio and optimizing their geometric parameters, namely pore size and filament thickness. Furthermore, given that the meshes were produced from polycaprolactone (PCL), a biodegradable and biocompatible polymer, it will be important to assess the influence of material degradation on their mechanical properties over time. Conducting in vitro and in vivo tests will also enable the study of cell adhesion, tissue integration and the biological performance of the structures under physiological conditions. Finally, the development of numerical models may complement the experimental results obtained and support the optimization of auxetic geometries for future applications in the treatment of pelvic organ prolapse.

In summary, this study demonstrated that auxetic PCL meshes have potential for application in the treatment of pelvic prolapse, combining flexibility and mechanical compatibility, but require geometric and experimental adjustments to achieve the structural effectiveness necessary for clinical use.

References

[1] K. J. Ko and K. S. Lee, “Current surgical management of pelvic organ prolapse: Strategies for the improvement of surgical outcomes,” *Investig. Clin. Urol.*, vol. 60, no. 6, pp. 413–424, 2019, doi: 10.4111/icu.2019.60.6.413.

[2] M. N. B. da Cunha, R. Rynkevic, M. E. T. da Silva, A. F. Moreira Da Silva Brandaõ, J. L. Alves, and A. A. Fernandes, “Melt Electrospinning Writing of Mesh Implants for Pelvic Organ Prolapse Repair,” *3D Print. Addit. Manuf.*, vol. 9, no. 5, pp. 389–398, 2022, doi: 10.1089/3dp.2021.0010.

[3] A. F. Hundley and S. Nekkanti, “Surgical management of pelvic organ prolapse,” *Gynecol. Care*, pp. 231–247, 2018, doi: 10.1017/9781108178594.025.

[4] J. M. P. Almeida, “Predicting the mechanical behaviour of the vaginal wall and mesh implants in ball burst tests,” Faculdade de Engenharia da Universidade do Porto, 2024.

[5] C. Saldanha, “Pelvic Organ Prolapse,” *Physician Assist. Clin.*, vol. 7, no. 3, pp. 485–497, 2022, doi: 10.1016/j.cpha.2022.03.003.

[6] A. S. Wanzeller and L. Soares De Sousa, “Drug-Coated Melt Electrowritten Mesh Implants for Pelvic Organ Prolapse Repair,” 2024.

[7] E. Mancuso, C. Downey, E. Doxford-Hook, M. G. Bryant, and P. Culmer, “The use of polymeric meshes for pelvic organ prolapse: Current concepts, challenges, and future perspectives,” *J. Biomed. Mater. Res. Part B Appl. Biomater.*, vol. 108, no. 3, pp. 771–789, Apr. 2020, doi: 10.1002/jbm.b.34432.

[8] F. Vaz *et al.*, “Innovative Melt-Electrowritten Mesh Implants with AntistaticProperties for Pelvic Organ Prolapse Repair,” *IUGA/EUGA Jt. Meet. 2025*, no. June, 2025.

[9] A. Y. Weintraub, H. Glinter, and N. Marcus-Braun, “Narrative review of the epidemiology, diagnosis and pathophysiology of pelvic organ prolapse,” *Int. Braz J Urol*, vol. 46, no. 1, pp. 5–14, 2020, doi: 10.1590/S1677-5538.IBJU.2018.0581.

[10] M. M. Bubakir, H. Li, and A. Barhoum, *Handbook of Nanofibers*, no. April 2018. 2020.

doi: 10.1007/978-3-319-42789-8.

[11] J. M. DeSilva and K. R. Rosenberg, "Anatomy, Development, and Function of the Human Pelvis," *Anat. Rec.*, vol. 300, no. 4, pp. 628–632, 2017, doi: 10.1002/ar.23561.

[12] R. F. Ferreira, "Development of a computational tool to simulate the use of synthetic meshes for pelvic organ prolapse repair," 2020.

[13] S. Paramasivam, A. Proietto, and M. Puvaneswary, "Pelvic anatomy and MRI," *Best Pract. Res. Clin. Obstet. Gynaecol.*, vol. 20, no. 1, pp. 3–22, 2006, doi: 10.1016/j.bpobgyn.2005.09.001.

[14] R. K. Kotarinos, *Musculoskeletal Pelvic Anatomy*. 2016. doi: 10.1016/B978-0-12-803228-2.00003-9.

[15] Z. Ghanbari *et al.*, "Quality of Life Following Pelvic Organ Prolapse Treatments in Women: A Systematic Review and Meta-Analysis," *J. Clin. Med.*, vol. 11, no. 23, p. 7166, Dec. 2022, doi: 10.3390/jcm11237166.

[16] J. F. Zhang *et al.*, "Investigation of the ischioanal fossa: Application to abscess spread," *Clin. Anat.*, vol. 30, no. 8, pp. 1029–1033, 2017, doi: 10.1002/ca.22901.

[17] D. Aldabe, N. Hammer, N. A. M. S. Flack, and S. J. Woodley, "A systematic review of the morphology and function of the sacrotuberous ligament," *Clin. Anat.*, vol. 32, no. 3, pp. 396–407, 2019, doi: 10.1002/ca.23328.

[18] H. Matsutani, G. Nakai, T. Yamada, K. Yamamoto, M. Ohmichi, and Y. Narumi, "Diversity of imaging features of ovarian sclerosing stromal tumors on MRI and PET-CT: A case report and literature review," *J. Ovarian Res.*, vol. 11, no. 1, pp. 4–8, 2018, doi: 10.1186/s13048-018-0473-1.

[19] A. Braga and M. Serati, "New Advances in Female Pelvic Floor Dysfunction Management," *Medicina (B. Aires).*, vol. 59, no. 6, p. 1010, May 2023, doi: 10.3390/medicina59061010.

[20] C. Maher, B. Feiner, K. Baessler, N. Haya, and J. Marjoribanks, "Transvaginal mesh or gra s compared with native tissue repair for vaginal prolapse (Review)," 2016, doi: 10.1002/14651858.CD012079.www.cochranelibrary.com.

[21] R. Gong and Z. Xia, "European Journal of Obstetrics & Gynecology and Reproductive Biology Collagen changes in pelvic support tissues in women with pelvic organ prolapse," vol. 234, pp. 185–189, 2019.

[22] T. Belayneh, A. Gebeyehu, M. Adefris, G. Rortveit, and J. L. Gjerde, "Pelvic organ

prolapse surgery and health - related quality of life : a follow - up study," pp. 1–11, 2021.

[23] F. Ergebnisse and T. Cadenbach-blome, "Significant Improvement in Quality of Life , Positive Effect on Sexuality , Lasting Reconstructive Result and Low Rate of Complications Following Cystocele Correction Using a Lightweight , Large-Pore , Titanised Polypropylene Mesh Final Results of a Natio," pp. 959–968, 2019.

[24] E. P. Ubertazzi, H. F. E. Soderini, A. J. M. Saavedra Sanchez, C. Fonseca Guzman, and L. I. Paván, "Long-term outcomes of transvaginal mesh (TVM) In patients with pelvic organ prolapse: A 5-year follow-up," *Eur. J. Obstet. Gynecol. Reprod. Biol.*, vol. 225, pp. 90–94, 2018, doi: 10.1016/j.ejogrb.2018.03.060.

[25] A. Gauthier, P. Ferry, P. Bertherat, R. De Tayrac, and H. Fernandez, "Transvaginal treatment of anterior and apical genital prolapse using Restorelle® direct fix™: An observational study of medium-term complications and outcomes," *J. Gynecol. Obstet. Hum. Reprod.*, vol. 49, no. 2, 2020, doi: 10.1016/j.jogoh.2019.101674.

[26] A. Bartuzi, K. Futyma, B. Kulik-Rechberger, and T. Rechberger, "Self-perceived quality of life after pelvic organ prolapse reconstructive mesh surgery: Prospective study," *Eur. J. Obstet. Gynecol. Reprod. Biol.*, vol. 169, no. 1, pp. 108–112, 2013, doi: 10.1016/j.ejogrb.2013.03.018.

[27] S. Todros, P. G. Pavan, and A. N. Natali, "Biomechanical properties of synthetic surgical meshes for pelvic prolapse repair," *J. Mech. Behav. Biomed. Mater.*, vol. 55, pp. 271–285, 2016, doi: 10.1016/j.jmbbm.2015.10.024.

[28] M. Yuan *et al.*, "Application of synthetic and natural polymers in surgical mesh for pelvic floor reconstruction," *Mater. Des.*, vol. 209, 2021, doi: 10.1016/j.matdes.2021.109984.

[29] E. Mancuso, C. Downey, E. Doxford-Hook, M. G. Bryant, and P. Culmer, "The use of polymeric meshes for pelvic organ prolapse: Current concepts, challenges, and future perspectives," *J. Biomed. Mater. Res. - Part B Appl. Biomater.*, vol. 108, no. 3, pp. 771–789, 2020, doi: 10.1002/jbm.b.34432.

[30] K. Baylón, P. Rodríguez-Camarillo, A. Elías-Zúñiga, J. A. Díaz-Elizondo, R. Gilkerson, and K. Lozano, "Past, present and future of surgical meshes: A review," *Membranes (Basel).*, vol. 7, no. 3, pp. 1–23, 2017, doi: 10.3390/membranes7030047.

[31] J. P. García-Ruíz and A. D. Lantada, "3D printed structures filled with carbon fibers and functionalized with mesenchymal stem cell conditioned media as in vitro cell niches for

promoting chondrogenesis," *Materials (Basel).*, vol. 11, no. 1, 2017, doi: 10.3390/ma11010023.

[32] R. Rynkevic, M. E. T. Silva, P. Martins, T. Mascarenhas, J. L. Alves, and A. A. Fernandes, "Characterisation of polycaprolactone scaffolds made by melt electrospinning writing for pelvic organ prolapse correction - a pilot study," *Mater. Today Commun.*, vol. 32, no. January, 2022, doi: 10.1016/j.mtcomm.2022.104101.

[33] M. Russo Serafini *et al.*, "3D-Printed Medical-Grade Polycaprolactone (mPCL) Scaffold for the Surgical Treatment of Vaginal Prolapse and Abdominal Hernias," *Bioengineering*, vol. 10, no. 11, p. 1242, Oct. 2023, doi: 10.3390/bioengineering10111242.

[34] K. M. Knight, P. A. Moalli, and S. D. Abramowitch, "Preventing Mesh Pore Collapse by Designing Mesh Pores with Auxetic Geometries: A Comprehensive Evaluation Via Computational Modeling," *J. Biomech. Eng.*, vol. 140, no. 5, pp. 1–8, 2018, doi: 10.1115/1.4039058.

[35] L.-M. Zhu, "Mesh implants: An overview of crucial mesh parameters," *World J. Gastrointest. Surg.*, vol. 7, no. 10, p. 226, 2015, doi: 10.4240/wjgs.v7.i10.226.

[36] M. Tutar, "A Comparative Evaluation of the Effects of Manufacturing Parameters on Mechanical Properties of Additively Manufactured PA and CF-Reinforced PA Materials," *Polymers (Basel).*, vol. 15, no. 1, p. 38, Dec. 2022, doi: 10.3390/polym15010038.

[37] R. Jose Varghese, E. H. M. Sakho, S. Parani, S. Thomas, O. S. Oluwafemi, and J. Wu, "Introduction to nanomaterials: Synthesis and applications," *Nanomater. Sol. Cell Appl.*, pp. 75–95, 2019, doi: 10.1016/B978-0-12-813337-8.00003-5.

[38] F. Afghah, C. Dikyol, M. Altunbek, and B. Koc, "Biomimicry in bio-manufacturing: Developments in melt electrospinning writing technology towards hybrid biomanufacturing," *Appl. Sci.*, vol. 9, no. 17, 2019, doi: 10.3390/app9173540.

[39] M. Pérez, D. Carou, E. M. Rubio, and R. Teti, "Current advances in additive manufacturing," *Procedia CIRP*, vol. 88, no. July 2019, pp. 439–444, 2020, doi: 10.1016/j.procir.2020.05.076.

[40] T. D. Ngo, A. Kashani, G. Imbalzano, K. T. Q. Nguyen, and D. Hui, "Additive manufacturing (3D printing): A review of materials, methods, applications and challenges," *Compos. Part B Eng.*, vol. 143, no. December 2017, pp. 172–196, 2018, doi: 10.1016/j.compositesb.2018.02.012.

[41] A. Youssef, S. J. Hollister, and P. D. Dalton, “Additive manufacturing of polymer melts for implantable medical devices and scaffolds,” *Biofabrication*, vol. 9, no. 1, 2017, doi: 10.1088/1758-5090/aa5766.

[42] N. Arifin, I. Sudin, N. H. A. Ngadiman, and M. S. A. Ishak, “A Comprehensive Review of Biopolymer Fabrication in Additive Manufacturing Processing for 3D-Tissue-Engineering Scaffolds,” *Polymers (Basel).*, vol. 14, no. 10, p. 2119, May 2022, doi: 10.3390/polym14102119.

[43] P. D. Dalton, “Melt electrowriting with additive manufacturing principles,” *Curr. Opin. Biomed. Eng.*, vol. 2, pp. 49–57, 2017, doi: 10.1016/j.cobme.2017.05.007.

[44] K. D. Patel, A. R. Padalhin, R. A. G. Franco, F. Verisqa, H. W. Kim, and L. Nguyen, *Basic concepts and fundamental insights into electrospinning*. 2021. doi: 10.1016/B978-0-12-822476-2.00010-8.

[45] R. Fernea, F. Babot, C. Munteanu, and R. Fernea, “ScienceDirect ScienceDirect ScienceDirect ScienceDirect Costing models for capacity optimization in Industry on the acoustic rehabilitation of a church between used capacity and operational efficiency,” *Procedia Manuf.*, vol. 00, no. 2017, pp. 392–399, 2018, [Online]. Available: https://doi.org/10.1016/j.promfg.2018.04.028

[46] N. Sheoran, B. Boland, S. Thornton, J. R. Bochinski, and L. I. Clarke, “Increasing ionic conductivity within thermoplasticsviacommercial additives results in a dramatic decrease in fiber diameter from melt electrospinning,” *Soft Matter*, vol. 17, no. 41, pp. 9264–9279, 2021, doi: 10.1039/d1sm01101d.

[47] J. Xue, T. Wu, Y. Dai, and Y. Xia, “Electrospinning and electrospun nanofibers: Methods, materials, and applications,” *Chem. Rev.*, vol. 119, no. 8, pp. 5298–5415, 2019, doi: 10.1021/acs.chemrev.8b00593.

[48] T. Matsuura and M. M. A. Shirazi, “Principles of electrospinning and nanofiber membranes,” in *Electrospun and Nanofibrous Membranes*, Elsevier, 2023, pp. 3–25. doi: 10.1016/B978-0-12-823032-9.00016-7.

[49] G. Hochleitner *et al.*, “Additive manufacturing of scaffolds with sub-micron filaments via melt electrospinning writing,” *Biofabrication*, vol. 7, no. 3, 2015, doi: 10.1088/1758-5090/7/3/035002.

[50] R. P. A. Hartman, D. J. Brunner, D. M. A. Camelot, J. C. M. Marijnissen, and B. Scarlett, “Electrohydrodynamic atomization in the cone-jet mode physical modeling of the liquid cone and jet,” *J. Aerosol Sci.*, vol. 30, no. 7, pp. 823–849, 1999, doi:

10.1016/S0021-8502(99)00033-6.

[51] T. D. Brown, P. D. Dalton, and D. W. Hutmacher, “Melt electrospinning today: An opportune time for an emerging polymer process,” *Prog. Polym. Sci.*, vol. 56, pp. 116–166, 2016, doi: 10.1016/j.progpolymsci.2016.01.001.

[52] Y. Xie, Q. Fang, H. Zhao, Y. Li, Z. Lin, and J. Chen, “Effects of Six Processing Parameters on the Size of PCL Fibers Prepared by Melt Electrospinning Writing,” *Micromachines*, vol. 14, no. 7, p. 1437, Jul. 2023, doi: 10.3390/mi14071437.

[53] Y. Jin *et al.*, “Fabrication of heterogeneous scaffolds using melt electrospinning writing: Design and optimization,” *Mater. Des.*, vol. 185, pp. 1–8, 2020, doi: 10.1016/j.matdes.2019.108274.

[54] F. M. Wunner, O. Bas, N. T. Saidy, P. D. Dalton, E. M. De-Juan Pardo, and D. W. Hutmacher, “Melt electrospinning writing of three-dimensional poly(ε-caprolactone) scaffolds with controllable morphologies for tissue engineering applications,” *J. Vis. Exp.*, vol. 2017, no. 130, 2017, doi: 10.3791/56289.

[55] S. Sterk, M. E. T. Silva, A. A. Fernandes, A. Huß, and A. Wittek, “Development of new surgical mesh geometries with different mechanical properties using the design freedom of 3D printing,” *J. Appl. Polym. Sci.*, no. September, pp. 1–15, 2023, doi: 10.1002/app.54687.

[56] E. H. Backes *et al.*, “Polycaprolactone usage in additive manufacturing strategies for tissue engineering applications: A review,” *J. Biomed. Mater. Res. - Part B Appl. Biomater.*, vol. 110, no. 6, pp. 1479–1503, 2022, doi: 10.1002/jbm.b.34997.

[57] J. Ren *et al.*, “Development of 3D Printed Biodegradable Mesh with Antimicrobial Properties for Pelvic Organ Prolapse,” *Polymers (Basel).*, vol. 14, no. 4, p. 763, Feb. 2022, doi: 10.3390/polym14040763.

[58] Y. Kim, K. H. Son, and J. W. Lee, “Auxetic Structures for Tissue Engineering Scaffolds and Biomedical Devices,” *Materials (Basel).*, vol. 14, no. 22, p. 6821, Nov. 2021, doi: 10.3390/ma14226821.

[59] K. W. Wojciechowski, “Poisson’s ratio of anisotropic systems,” *Comput. Methods Sci. Technol.*, vol. 11, no. 1, pp. 73–79, 2005, doi: 10.12921/cmst.2005.11.01.73-79.

[60] E. Science and G. Britain, “chiral honeycombe. Poisson’s ratio. 1. INTRODUCTION Cellular solids are used widely in a variety of engineering applications. In particular,” *Science (80-.).*, vol. 39, no. 3, 1997.

[61] J. N. Grima and K. E. Evans, “Auxetic behavior from rotating triangles,” *J. Mater. Sci.*, vol. 41, no. 10, pp. 3193–3196, 2006, doi: 10.1007/s10853-006-6339-8.

[62] Y. Liu and H. Hu, “A review on auxetic structures and polymeric materials,” *Sci. Res. Essays*, vol. 5, no. 10, pp. 1052–1063, 2010.

[63] P. S. Theocaris, G. E. Stavroulakis, and P. D. Panagiotopoulos, “Negative Poisson’s ratios in composites with star-shaped inclusions: A numerical homogenization approach,” *Arch. Appl. Mech.*, vol. 67, no. 4, pp. 274–286, 1997, doi: 10.1007/s004190050117.

[64] J. N. Grima, R. Gatt, A. Alderson, and K. E. Evans, “On the potential of connected stars as auxetic systems,” *Mol. Simul.*, vol. 31, no. 13, pp. 925–935, 2005, doi: 10.1080/08927020500401139.

[65] C. W. Smith, J. N. Grima, and K. E. Evans, “Novel mechanism for generating auxetic behaviour in reticulated foams: Missing rib foam model,” *Acta Mater.*, vol. 48, no. 17, pp. 4349–4356, 2000, doi: 10.1016/S1359-6454(00)00269-X.

[66] N. Gaspar, X. J. Ren, C. W. Smith, J. N. Grima, and K. E. Evans, “Novel honeycombs with auxetic behaviour,” *Acta Mater.*, vol. 53, no. 8, pp. 2439–2445, 2005, doi: 10.1016/j.actamat.2005.02.006.

[67] W. J. S. Dolla, B. A. Fricke, and B. R. Becker, “Structural and drug diffusion models of conventional and auxetic drug-eluting stents,” *J. Med. Devices, Trans. ASME*, vol. 1, no. 1, pp. 47–55, 2007, doi: 10.1115/1.2355691.

[68] J. N. Grima, R. Gatt, and P. S. Farrugia, “On the properties of auxetic meta-tetrachiral structures,” *Phys. Status Solidi Basic Res.*, vol. 245, no. 3, pp. 511–520, 2008, doi: 10.1002/pssb.200777704.

[69] M. H. Fu, B. Bin Zheng, and W. H. Li, “A novel chiral three-dimensional material with negative Poisson’s ratio and the equivalent elastic parameters,” *Compos. Struct.*, vol. 176, pp. 442–448, 2017, doi: 10.1016/j.compstruct.2017.05.027.

[70] J. N. Grima, A. Alderson, and K. E. Evans, “Auxetic behaviour from rotating rigid units,” *Phys. status solidi*, vol. 242, no. 3, pp. 561–575, Mar. 2005, doi: 10.1002/pssb.200460376.

[71] A. Alderson and K. E. Evans, “Molecular Origin of Auxetic Behavior in Tetrahedral Framework Silicates,” *Phys. Rev. Lett.*, vol. 89, no. 22, p. 225503, Nov. 2002, doi: 10.1103/PhysRevLett.89.225503.

[72] R. Gatt *et al.*, “Hierarchical Auxetic Mechanical Metamaterials,” *Sci. Rep.*, vol. 5, pp. 1–6, 2015, doi: 10.1038/srep08395.

[73] P. Soman, J. W. Lee, A. Phadke, S. Varghese, and S. Chen, “Spatial tuning of negative and positive Poisson’s ratio in a multi-layer scaffold,” *Acta Biomater.*, vol. 8, no. 7, pp. 2587–2594, 2012, doi: 10.1016/j.actbio.2012.03.035.

[74] W. Zhang, P. Soman, K. Meggs, X. Qu, and S. Chen, “Tuning the poisson’s ratio of biomaterials for investigating cellular response,” *Adv. Funct. Mater.*, vol. 23, no. 25, pp. 3226–3232, 2013, doi: 10.1002/adfm.201202666.

[75] N. Easey *et al.*, “Dome-shape auxetic cellular metamaterials: Manufacturing, modeling, and testing,” *Front. Mater.*, vol. 6, no. April, pp. 1–13, 2019, doi: 10.3389/fmats.2019.00086.

[76] M. Attar, S. S. Aydin, A. Arabaci, and I. Mutlu, “Mechanical meta-material-based polymer skin graft production by rapid prototyping and replica method,” *Rapid Prototyp. J.*, vol. 27, no. 2, pp. 278–287, 2021, doi: 10.1108/RPJ-12-2019-0307.

[77] A. Muslija and A. Díaz Lantada, “Deep reactive ion etching of auxetic structures: Present capabilities and challenges,” *Smart Mater. Struct.*, vol. 23, no. 8, 2014, doi: 10.1088/0964-1726/23/8/087001.

[78] A. D. Lantada, A. Muslija, and J. P. Garcia-Ruiz, “Auxetic tissue engineering scaffolds with nanometric features and resonances in the megahertz range,” *Smart Mater. Struct.*, vol. 24, no. 5, 2015, doi: 10.1088/0964-1726/24/5/055013.

[79] S. K. Bhullar *et al.*, “Design and fabrication of auxetic PCL nanofiber membranes for biomedical applications,” *Mater. Sci. Eng. C*, vol. 81, no. June, pp. 334–340, 2017, doi: 10.1016/j.msec.2017.08.022.

[80] S. Burns, “Negative Poisson’s Ratio Materials,” *Science (80-.).*, vol. 238, no. 4826, pp. 551–551, Oct. 1987, doi: 10.1126/science.238.4826.551.a.

[81] Z. Wang and H. Hu, “Tensile and forming properties of auxetic warp-knitted spacer fabrics,” *Text. Res. J.*, vol. 87, no. 16, pp. 1925–1937, 2017, doi: 10.1177/0040517516660889.

[82] Z. Ge and H. Hu, “A theoretical analysis of deformation behavior of an innovative 3D auxetic textile structure,” *J. Text. Inst.*, vol. 106, no. 1, pp. 101–109, 2015, doi: 10.1080/00405000.2014.906099.

[83] H. I. Ahmed, M. Umair, Y. Nawab, and S. T. A. Hamdani, “Development of 3D auxetic

structures using para-aramid and ultra-high molecular weight polyethylene yarns," *J. Text. Inst.*, vol. 112, no. 9, pp. 1417–1427, 2021, doi: 10.1080/00405000.2020.1819007.

[84] J. J. Warner, A. R. Gillies, H. H. Hwang, H. Zhang, R. L. Lieber, and S. Chen, "3D-printed biomaterials with regional auxetic properties," *J. Mech. Behav. Biomed. Mater.*, vol. 76, no. May, pp. 145–152, 2017, doi: 10.1016/j.jmbbm.2017.05.016.

[85] J. W. Lee, P. Soman, J. H. Park, S. Chen, and D. W. Cho, "A tubular biomaterial construct exhibiting a negative poisson's ratio," *PLoS One*, vol. 11, no. 5, pp. 1–14, 2016, doi: 10.1371/journal.pone.0155681.

[86] M. V. Deshpande, A. J. West, S. H. Bernacki, K. Luan, and M. W. King, "Poly(ε-caprolactone) resorbable auxetic designed knitted scaffolds for craniofacial Skeletal muscle regeneration," *Bioengineering*, vol. 7, no. 4, pp. 1–15, 2020, doi: 10.3390/bioengineering7040134.

[87] J. Dirrenberger, S. Forest, and D. Jeulin, "Effective elastic properties of auxetic microstructures: Anisotropy and structural applications," *Int. J. Mech. Mater. Des.*, vol. 9, no. 1, pp. 21–33, 2013, doi: 10.1007/s10999-012-9192-8.

[88] N. C. Paxton, R. Daley, D. P. Forrestal, M. C. Allenby, and M. A. Woodruff, "Auxetic tubular scaffolds via melt electrowriting," *Mater. Des.*, vol. 193, pp. 4–6, 2020, doi: 10.1016/j.matdes.2020.108787.

[89] Y. ching Keung, K. lun Yick, A. Yu, and J. Yip, "Exploring re-entrant auxetic silicone structures to design bra pads," *Polym. Test.*, vol. 135, no. April, 2024, doi: 10.1016/j.polymertesting.2024.108462.

[90] M. A. Woodruff and D. W. Hutmacher, "The return of a forgotten polymer - Polycaprolactone in the 21st century," *Prog. Polym. Sci.*, vol. 35, no. 10, pp. 1217–1256, 2010, doi: 10.1016/j.progpolymsci.2010.04.002.

[91] R. Patel, D. Monticone, M. Lu, L. Grøndahl, and H. Huang, "Hydrolytic degradation of porous poly(hydroxybutyrate-co-hydroxyvalerate) scaffolds manufactured using selective laser sintering," *Polym. Degrad. Stab.*, vol. 187, 2021, doi: 10.1016/j.polymdegradstab.2021.109545.

[92] M. N. Cunha, "Optimisation of a MEW prototype for mesh implants fabrication," 2020.

[93] J. N. Grima, R. Cauchi, R. Gatt, and D. Attard, "Honeycomb composites with auxetic out-of-plane characteristics," *Compos. Struct.*, vol. 106, pp. 150–159, 2013, doi: 10.1016/j.compstruct.2013.06.009.

[94] N. M. Ferreira *et al.*, "Melt Electrowritten Biodegradable Mesh Implants with Auxetic Designs for Pelvic Organ Prolapse Repair," *J. Manuf. Mater. Process.*, vol. 9, no. 4, pp. 1–13, 2025, doi: 10.3390/jmmp9040111.

[95] C. Soares, P. Martins, E. Silva, L. Hympanova, and R. Rynkevic, "Cog Threads for Transvaginal Prolapse Repair: Ex-Vivo Studies of a Novel Concept," *Surgeries*, vol. 3, no. 2, pp. 101–110, May 2022, doi: 10.3390/surgeries3020012.

Contribution to the Sustainable Development Goals (SDGs)

The present work is aligned with the United Nations Sustainable Development Goals (SDGs), contributing primarily to SDG 3 – Good Health and Well-Being and SDG 9 – Industry, Innovation and Infrastructure. This contribution arises from the development and mechanical characterization of biodegradable auxetic meshes intended for potential applications in the treatment of pelvic organ prolapse, promoting both technological innovation and the improvement of patients' quality of life.

"SDG 3 – Good Health and Well-Being" aims to ensure healthy lives and promote well-being for all at all ages. In this context, the present research contributes to the development of potential therapeutic solutions for the treatment of pelvic organ prolapse, a condition that significantly affects the quality of life of millions of women worldwide. The development and characterization of biodegradable polycaprolactone (PCL) meshes, designed to provide mechanical support to vaginal tissue while reducing the complications associated with conventional synthetic meshes, directly supports this objective. The most relevant target associated with this work is the promotion of health and well-being through the development of safer and more effective medical technologies. Performance indicators associated with this contribution include the experimentally determined mechanical properties of the developed structures, namely their ability to reinforce vaginal tissue, their mechanical strength, and their biomechanical compatibility with soft biological tissues.

"SDG 9 – Industry, Innovation and Infrastructure" seeks to foster scientific research, technological innovation, and sustainable industrial development. This study contributes to this objective through the application of Melt Electrowriting (MEW), an advanced additive manufacturing technology, for the fabrication of innovative auxetic structures intended for biomedical applications. The design and characterization of these geometries represent an innovative approach to the development of implantable devices with mechanical properties tailored to the physiological requirements of vaginal tissue. Within this framework, the most relevant target relates to strengthening scientific research and enhancing technological innovation. Performance indicators include the development of novel auxetic geometries, their mechanical characterization, and the experimental demonstration of their ability to provide mechanical reinforcement to vaginal tissue.

Furthermore, the use of polycaprolactone, a biodegradable and biocompatible polymer, represents an additional contribution towards the development of more sustainable biomedical solutions. By enabling the fabrication of temporary implants capable of gradually degrading after fulfilling their therapeutic function, PCL offers a promising alternative to permanent synthetic materials traditionally employed in pelvic floor repair.

Overall, this dissertation demonstrates how biomedical engineering can contribute to the achievement of the Sustainable Development Goals through the integration of scientific research, technological innovation, and the development of advanced healthcare solutions aimed at improving human health and well-being.